A full degree-of-freedom spatiotemporal light modulator

Christopher L. Panuski*[1], Ian R. Christen[1], Momchil Minkov[2], Cole J. Brabec[1], Sivan Trajtenberg-Mills[1], Alexander D. Griffiths[3], Jonathan J.D. McKendry[3], Gerald L. Leake[4], Daniel J. Coleman[4], Cung Tran[4], Jeffrey St Louis[4], John Mucci[4], Cameron Horvath[5], Jocelyn N. Westwood-Bachman[5], Stefan F. Preble[6], Martin D. Dawson[3], Michael J. Strain[3], Michael L. Fanto[7], and Dirk R. Englund†[1]

[1]Research Laboratory of Electronics, Massachusetts Institute of Technology, Cambridge, MA 02139, USA

[2]Flexcompute, Inc., 130 Trapelo Rd., Belmont, MA 02478, USA

[3]Institute of Photonics, Dept. of Physics, University of Strathclyde, Technology and Innovation Centre, Glasgow G1 1RD, UK

[4]State University of New York Polytechnic Institute, Albany, NY 12203, USA

[5]Applied Nanotools, Inc., Edmonton, AB T6G2M9, CA

[6]Microsystems Engineering, Rochester Institute of Technology, Rochester, NY 14623, USA

[7]Air Force Research Laboratory, Information Directorate, Rome, NY, 13441, USA

August 25, 2022

Abstract

Harnessing the full complexity of optical fields requires complete control of all degrees-of-freedom within a region of space and time — an open goal for present-day spatial light modulators (SLMs), active metasurfaces, and optical phased arrays. Here, we solve this challenge with a programmable photonic crystal cavity array enabled by four key advances: (i) near-unity vertical coupling to high-finesse microcavities through inverse design, (ii) scalable fabrication by optimized, 300 mm full-wafer processing, (iii) picometer-precision resonance alignment using automated, closed-loop "holographic trimming", and (iv) out-of-plane cavity control via a high-speed µLED array. Combining each, we demonstrate near-complete spatiotemporal control of a 64-resonator, two-dimensional SLM with nanosecond- and femtojoule-order switching. Simultaneously operating wavelength-scale modes near the space- and time-bandwidth limits, this work opens a new regime of programmability at the fundamental limits of multimode optical control.

Programmable optical transformations are of fundamental importance across science and engineering, from adaptive optics in astronomy [1] and neuroscience [2, 3] to dynamic matrix operations in machine learning [4–6] and quantum computing [7, 8]. Despite this importance, high-resolution manipulation of multimode optical fields — the central objective of spatial light modulators (SLMs) — remains an open challenge [9]. Specifically, the limited modulation bandwidth and/or pixel density of liquid crystal- or micromirror-based SLMs [10, 11], optical phased arrays [12, 13], and active metasurfaces [14–17] prevent complete control of the optical fields they tune [18].

Figure 1a illustrates the limitations of current SLMs, which typically comprise a two-dimensional (2D), Λ-pitch array of tunable pixels (subscript p) emitting at wavelength λ into the solid angle Ω_p with a system (subscript s) modulation bandwidth ω_s. Given these parameters, each "spatiotemporal" degree-of-freedom (DoF) simultaneously satisfying the minimum-uncertainty space- and time-bandwidth relations

*Corresponding Author: cpanuski@mit.edu

†Corresponding Author: englund@mit.edu

This is a peer reviewed accepted manuscript of the following research article:
Panuski, C. L., Christen, I., Minkov, M., Brabec, C. J., Trajtenberg-Mills, S., Griffiths, A. D., McKendry, J. J. D., Leake, G. L., Coleman, D. J., Tran, C., St. Louis, J., Horvath, C., Westwood-Bachman, J. N., Preble, S. F., Dawson, M. D., Strain, M. J., Fanto, M. L., & Englund, D. R. (2022). A full degree-of-freedom spatiotemporal light modulator. Nature Photonics, 16, 834–842. https://doi.org/10.1038/s41566-022-01086-9

($\delta A/\lambda^2 \cdot \delta\Omega = 1$ and $\delta t \cdot \delta\omega = 1$, respectively) can be illustrated as a real-space voxel with area λ^2/Ω_p and time duration $1/\omega_p$ for pixel bandwidth ω_p. The optical-delay-limited pixel bandwidth $\omega_p \approx (\Delta\epsilon_p/\epsilon)ck$ can be approximated perturbatively as a function of the achievable permittivity swing $\Delta\epsilon_p$ (for the speed of light c) or similarly derived from linear scattering theorems [19].

Integrating over the switching interval $T = 1/\omega_s$ and aperture area A then gives the total DoF count [18]

$$F = \int_{A,\Omega_p} \frac{\mathrm{d}A}{\lambda^2} \cdot \mathrm{d}\Omega \int_{T,\omega_p} \mathrm{d}t \cdot \mathrm{d}\omega. \tag{1}$$

By comparison, the same switching period contains $N = A/\Lambda^2 \leq F$ *controllable* modes, each confined to the pixel area Λ^2 and time window T (shaded box in Fig. 1a). Complete spatiotemporal control with $N = F$ is only achieved under the following criteria: (C1) emitters fully "fill" the near-field aperture such that Ω_p matches the field-of-view $\Omega_s = (\lambda/\Lambda)^2$ of a single array diffraction order; and (C2) $\omega_s = \omega_p$. In the Fourier domain, the system's "spatiotemporal bandwidth" $\nu = \Omega_s\omega_s$ counts the controllable DoF per unit area and time within a single far-field diffraction order. As illustrated by the shaded pillbox in Fig. 1a, (C1) and (C2) are both satisfied when ν matches the accessible pixel bandwidth $\Omega_p\omega_p$.

Practical constraints have prevented present-day SLM technology from achieving this bound (Methods). Figure 1b compares the performance of various experimentally-demonstrated, active, 2D SLMs as a function of spatiotemporal bandwidth's two components: modulation bandwidth ω_s and field-of-view Ω_s. Controllability aside, the evident trade-off between these parameters illustrates the difficulty of creating fast, compact modulator arrays with high ν. Thus, in addition to satisfying the complete control criteria (C1) and (C2), an "ideal" SLM would: (C3) maximize ν by combining wavelength-scale pitches (for full-field $\Omega_s \to 2\pi$ beamforming) with gigahertz (GHz)-order bandwidths ω_s competitive with electronic processors; (C4) support femtojoule (fJ)-order switching energies as desired for information processing applications [20]; and (C5) have scalability to state-of-the-art megapixel-scale apertures.

These criteria motivate the resonant architecture in Fig. 1c. Here, (C3) and (C4) are achieved by switching a fully-filled array of wavelength-scale resonant optical antennas with fast, fJ-order perturbations $\Delta\epsilon_p/\epsilon \ll 1$. Each resonator's far-field scattering and quality factor Q can then be tuned to achieve (C1) and (C2), respectively. *Combined, this resonant SLM architecture enables complete, efficient control of the large spatiotemporal bandwidth supported by its constituent pixels.*

Figure 2 illustrates our specific implementation of this full-DoF resonant SLM: the photonic crystal spatial light modulator (PhC-SLM) [21]. Coherent signal light is reflected off a semiconductor slab (permittivity ϵ) hosting a 2D array of semiconductor PhC cavities with instantaneous resonant frequency $\omega_0 + \Delta_{mn}(t)$. A short-wavelength incoherent control plane imaged onto the cavity array controls each resonator's detuning $\Delta_{mn}(t) \approx -\Delta\epsilon(t)/2\epsilon$ via the permittivity change $\Delta\epsilon_p(t)$ induced by photo-excited free carriers [22]. We optimize the resonator bandwidth $\Gamma \approx \omega_s \approx 2\pi \times$ GHz (corresponding to a quality factor $Q = \omega_0/\Gamma \sim 10^5$) to maximize the linewidth-normalized detuning Δ/Γ without significantly attenuating the cavity's response at the carrier lifetime (τ)-limited modulation rate $\omega_s = 1/\tau$. By engineering the cavity's coupling regime and associated complex reflectivity $r(\Delta)$, the resulting linewidth-order detunings enable phase-dominant, amplitude-dominant, or coupled amplitude-phase modulation with negligible free carrier absorption. Free carrier dispersion thereby enables fast (> 100 MHz given a $\sim$ns free carrier lifetime [23]), low-energy (fJ-order) conversion of incoherent control light into a dense array of coherent, modulated signal modes (Supplement Section A) [24].

This out-of-plane, all-optical switching approach is motivated by the recent development of high-speed, high-brightness µLED arrays [25, 26] integrated with complementary metal-oxide-semiconductor (CMOS) drive electronics for consumer displays [27, 28] and high-speed visible light communication [29, 30]. In particular, gallium nitride µLED arrays with GHz-order modulation bandwidths [30, 31], sub-micron pixel pitches [32], and large pixel counts [33] have been demonstrated within the past few years. Applying these arrays for reconfigurable, "wireless" all-optical cavity control eliminates electronic tuning elements at each pixel to avoid optical loss, pixel pitch limitations, and interconnect bottlenecks for planar architectures (as aperture area A grows, $\mathcal{O}(A)$ pixel controls eventually cannot be routed through the $\mathcal{O}(\sqrt{A})$ perimeter)

[34].

Free of these constraints, we designed high-finesse, vertically-coupled microcavities offering coupling efficiencies $> 90\%$, phase-dominant reflection spectra [35, 36], and directional emission $\Omega_p \approx \Omega_s$ for high-efficiency beamforming (Section 1). Bespoke, wafer-scale processing allows us to fabricate these "resonant antennas" in arrays with mean quality factors $\langle Q \rangle > 10^6$ and sub-nm resonant wavelength standard deviation (Section 2). For fine tuning, we developed a parallel laser-assisted thermal oxidation [37, 38] protocol to then trim 8×8 cavity arrays to picometer-order uniformity (Section 3), enabling high-speed spatial light modulation with fJ-order switching energies and $\omega_s > 2\pi \times 100$ MHz (Section 4). Compared to the previous devices surveyed in Fig. 1b, our PhC-SLM offers near-complete control over an order-of-magnitude larger spatiotemporal bandwidth.

1 Inverse-Designed Resonant Pixels

The sub-wavelength (i.e. normalized volume $\tilde{V} = V/(\lambda/n)^3 < 1$ relative to a cubic wavelength in the confining dielectric of refractive index n), high-Q modes of 2D PhC cavities enable (C4) [39], but at the expense of (C1) since Q optimization – via computationally expensive finite-difference time-domain (FDTD) simulations – cancels radiative leakage. Compared to the ideal apertures in Fig. 1c, these Q-optimized unit cells (i.e. pixels) confine a spatially complex mode with $\Omega_p \gg \Omega_s$ and near-zero η_0 (Methods).

Fortunately, this limitation is not fundamental: modified hole configurations can resonantly scatter the mode's evanescent field to produce a desired far-field emission pattern. One established design is the addition of a harmonic $2a$-period grating perturbation (Fig. 3a) that "folds" energy concentrated at the band-edge $k_x = \pi/a$ back to $k_{||} = 0$, yielding vertical radiation at the expense of reduced Q [40–43]. In the perturbative regime, the far-field scattering profile is an image of the broad band-edge mode. Thus, once the grating-induced loss becomes dominant, further magnifying the perturbation reduces Q without significantly improving directivity. Fig. 3b shows the narrowed far-field profile produced by a $\delta r_i/r \approx 0.02$ grating perturbation, which balances the reduced $Q \approx 8 \times 10^5$ with a modest diffraction efficiency improvement ($\eta_0 = 0.18$; c.f. $Q \approx \times 10^6$ and $\eta_0 = 0.04$ for the original design in Fig. E1).

By contrast, our design strategy combines semi-analytic guided mode expansion (GME) simulations with automatic differentiation to maximize η_0 (and thereby the effective near-field fill factor) for any given target Q using *all* of the hole parameters (Methods). The resulting designs support tunable-Q resonances with near-diffraction-limited ($\Omega_p \approx \Omega_p$) vertical beaming comparable to the ideal planar apertures of Fig. 1c. The example design of Fig. 3d, for instance, maintains $Q \approx 8 \times 10^5$ with $\eta_0 = 0.86$ based on the simulated far-field profile in Fig. 3e.

We prototyped each design at a commercial electron beam lithography (EBL) foundry (Applied Nanotools) before transitioning to the wafer-scale foundry process described in Sec. 2. The near- and far-field reflection characteristics of the fabricated devices were measured with a cross-polarized microscopy setup (Methods). Fig. 3b-c and Fig. 3e-f show the results for the grating coupled and inverse-designed cavities, respectively. The optimal grating-coupled cavities offer $Q \sim 4 \times 10^5$ at $\lambda \approx 1553$ nm with a near-field resonant scattering profile well-centered on the cavity defect (Fig. 3c, inset). The mode mismatch between this wavelength-scale PhC mode and the wide-field input beam (Gaussian beam with ∼150 µm waist diameter for array-level excitation) is further evidenced by the small normalized reflection amplitude (relative to that of the inverse designed cavities) on resonance as well as the broad far-field profile (Fig. 3b) with $\eta_0 = 0.24$.

By comparison, inverse design non-perturbatively modifies the cavity mode (Fig. 3d) to produce the near-ideal measured far-field profile in Fig. 3e satisfying (C1) with $\eta_0 = 0.98$ while *simultaneously* increasing Q to 5.7×10^5. We attribute the slight increase in zero-order diffraction efficiency over the simulated value $\eta_0 = 0.86$ to the substrate-dependent effects described in Supplement Section E. The fully-filled near-field resonant scattering image in Fig. 3f explains the close resemblance between this measured $S(\vec{k})$ and that of an ideal uniform aperture [44]. In addition, the narrowed emission profile yields a ∼5× increase in cross-polarized reflection and the phase-dominant simulated direct reflection spectrum in Fig. 3f. The latter is achieved by 94% one-sided coupling to a Gaussian beam with optimized waist diameter (Supplement Section C).

Combined, these results break the traditional coupling–Q tradeoff (offering an order-of-magnitude improvement in the figure-of-merit $\eta_0 \cdot Q$ for the prototype devices in Fig. 3) to enable high-performance beamforming at the space-bandwidth limit (C1).

2 Foundry-Fabricated High-Finesse Microcavity Arrays

While EBL enables fabrication of these few-pixel prototypes with state-of-the-art resolution and accuracy, serial direct-write techniques do not satisfy (C5). Field stitching issues and sample preparation aside, a single cm^2, megapixel-scale sample would require a full day of EBL write time alone. We therefore developed a full-wafer deep-ultraviolet photolithography process specifically optimized for wavelength-pitch arrays of high-Q/V PhC microcavities in a commercial foundry [45].

A central goal was to create vertical etch side-walls. The transmission electron microscope (TEM) cross-section in Fig. 4i shows that the default fabrication process (optimized for isolated waveguides) yielded an oblique (100°), incomplete etch through the silicon device layer for the target PhC lattice parameters. Both nonidealities erase the membrane's vertical reflection symmetry, leading to coupling between even- and odd- symmetry (about the slab midplane) modes that ultimately limits the achievable Q of bandgap-confined resonances [46]. By contrast, our revised fabrication process achieves near-vertical 91° sidewall angles (Fig. 4ii), yielding high-quality PhC lattices for a range of hole diameters between the $\sim$100 nm critical-dimension and $2r \approx a$ (Fig. 4c). Using TEM cross-sectioning and automated optical metrology as feedback over multiple 300 mm wafer runs in the *AIM Photonics* foundry's 193 nm DUV water-immersion lithography line, this new process relies on a combination of dose-optimized reverse- (positive-) tone lithography, high-accuracy laser written masks, and optimized etch termination. Following fabrication and dicing, we post-processed individual die with a backside silicon nitride anti-reflection coating and, as required, suspended the PhC membranes with a timed wet etch (Supplement Section E).

The resulting die contain isolated and arrayed PhC cavities with swept dimensions to offset systematic fabrication biases. We chose Lm-type cavity designs — formed by removing m holes from the PhC lattice as demonstrated by the $L3$ pixels in Fig. 3 — to host tunable-volume (via variable m), high-Q resonant modes with even reflection symmetry (about the pixel axes) as required for vertical emission [47]. The highest-performance isolated devices feature $Q > 10^6$ with normalized volumes $\tilde{V} \approx 0.3$. With a joint spectral- and spatial-confinement (quantified by the figure-of-merit $Q/\tilde{V}$) $\approx 4 \times 10^6$, these devices are among the highest-finesse optical cavities ever fabricated in a foundry process.

Our optimized foundry processing extends this exceptional single-device performance (rivaling record EBL-fabricated devices) to large-scale cavity arrays with near-unity yield. We developed a fully-automated measurement system to locate and characterize hundreds of cavities per second via parallel camera readout (Methods). The resulting data, extracted from over 10^5 devices measured across the wafer, allow us to statistically analyze resonator performance and fabrication variability at the die, reticle, and wafer level. Fig. 4d, for example, shows resonant wavelength and Q variations within 8×8 arrays of four different cavity designs. Using camera readout of the reflected wide-field excitation, each data set is extracted from a single wavelength scan of a tunable laser. Besides the expected correlation between uniformity and mode volume [48], the data demonstrates the ability to fabricate sub-wavelength ($\tilde{V} < 1$) microcavity arrays with $\langle Q \rangle > 10^6$ and sub-nanometer resonant wavelength standard deviation ($\sigma_\lambda \approx 0.6$ nm). Critically for beamforming, this uniformity also extends to the far-field: Fig. E4 shows that each cavity in an 8×8 array emits vertically with $\eta_0 = 0.86 \pm 0.07$, in quantitative agreement with the simulated result in Fig. 3.

3 Holographic Trimming

In addition to these overlapping far-field emission profiles, programmable multimode interference requires each cavity to operate near a common resonant wavelength λ_0. For sufficiently high-Q resonators, this tolerance cannot be solely achieved through optimized fabrication since $\mathcal{O}$(nm) fabrication fluctuations translate to $\mathcal{O}$(nm) resonant wavelength variations [49, 50]. Our prototype 8×8 arrays of $L3$ cavities (chosen to optimally balance requirements on Q, V, directive emission, and fabrication tolerance) typically span a $\sim$3 nm peak-to-peak wavelength variation (given $\sigma_\lambda \approx 0.6$ nm), corresponding to hundreds of linewidths for the target $Q \sim 10^5$.

To correct this nonuniformity, we developed an automated, low-loss, and picometer-precision trimming procedure based on laser-assisted thermal oxidation (Fig. 5). Two features of our approach resolve the speed and controllability limitations of prior single-device implementations [37, 38]: 1) accelerated oxidation in a high-pressure chamber with in-situ characterization; and 2) holographic fanout of the trimming laser to simultaneously address multiple devices (Methods).

Fig. 5 demonstrates the results of this trimming procedure applied to our prototype 8×8 pixel PhC-SLM. Prior to trimming, the hyperspectral near-field reflection image in Fig. 5c shows the large (> 200 linewidths for the mean quality factor $\langle Q \rangle = 1.6 \times 10^5$) resonant wavelength variation between the otherwise spatially uniform and high-fill resonant modes. Holographic trimming reduces the wavelength standard deviation and peak-to-peak spread by $> 100\times$ to $\sigma_\lambda = 2.5$ pm and $\Delta\lambda_0^{\text{p-p}} = 1.3\Gamma = 13$ pm, respectively, enabling all 64 devices (imaged in Fig. 5d) to be resonantly excited at a common operating wavelength (Fig. 5e). Since σ_λ is directly related to the corresponding hole radius and placement variability σ with an $\mathcal{O}(1)$ design-dependent constant of proportionality, the thermal oxide homogenizes the effective dimensions of each microcavity to the picometer scale. The mean quality factor and near-field reflection profile of the array remain largely unmodified throughout the process as evidenced by Fig. 5c and Fig. 5e.

To our knowledge, these results are the first demonstration of parallel, in situ, non-volatile microcavity trimming. The achievable scale is currently limited by environmental factors that could be overcome with stricter process control. Even without these improvements, the current uniformity, scale, and induced loss outperform the corresponding metrics of previous techniques (reviewed in Table E2), paving the way towards scalable integrated photonics with high-Q resonators.

4 All-Optical Spatial Light Modulation

Once trimmed to within a linewidth, each resonator reflects an incident coherent field $E_\text{i}(\vec{r}, t)$, producing a far-field output [51]

$$E_\text{r}(\vec{k}, t) = S(\vec{k}) \sum_{m,n} r\{\Delta_{mn}(t)\} E_\text{i}(\vec{r}_{mn}, t) e^{j\vec{k}\cdot\vec{r}_{mn}} \tag{2}$$

that can be dynamically controlled within $S(\vec{k})$ by setting the detuning $\Delta_{mn}(t)$ (and therefore the near-field reflection coefficient r) of each resonator. Experimentally, we measure the intensity pattern $|E_r(\vec{k})|^2$ on the back focal plane of a microscope objective above the temperature-stabilized PhC-SLM (to enable operation without laser-cavity locking) and optically program $\Delta_{mn}(t)$ via photo-excited free carriers (Methods).

Absent a control input ($\Delta_{mn} \approx 0$), Fig. 6d shows the static far-field intensity pattern $|E_r(\vec{k})|^2$ of a wide-field-illuminated, 8×8 trimmed array with $\langle Q \rangle = 1.85 \times 10^5$ and $\sigma_\lambda = 5$ pm at $\lambda = 1562$ nm. The inverse-designed pixels minimize scattering into undesired diffraction orders, producing a high-efficiency ($\eta_0 = 0.66$) zero-order beam with the expected 1.3° and 1.6° horizontal and vertical beamwidths given the $42.0\lambda \times 36.4\lambda$ aperture size. The cross-sectional beam profiles are well matched to the simulated emission profile of uniform apertures with width $w = 0.8\lambda$, suggesting an 80% effective linear fill of the array. This extracted value agrees with the observed zero-order efficiency and the array's physical design (each $16a \times 16a$ cavity offering near-unity fill was padded to $20a \times 20a$ to limit coupling to adjacent pixels).

After confirming the static performance of the array, we conducted optical switching experiments with two sources: an incoherent μLED array and a pulsed visible laser. The μLED array contains 16×16 individually-addressable gallium nitride μLEDs with >150 MHz small-signal bandwidth and $\sim 10^6$ cd/m^2 peak luminances (at 450 nm) flip-chip bonded to high-efficiency CMOS drivers [29, 52]. Digitally triggering the CMOS-controlled, 100 μm-pitch array (imaged with variable demagnification and rotation onto the PhC cavity array) then enables reconfigurable, binary optical addressing as illustrated by the imaged projections of three letters on the PhC-SLM (Fig. 6a). We measured the resulting pixel reflection amplitude and phase using locked, shot-noise-limited balanced homodyne detection (Methods). Fig. 6a depicts the maximum phase shift $\Delta\phi$ as a function of CMOS trigger duration T_{CMOS} and imaged pump energy density $E_{\mu\text{LED}}$. Single-cavity switching with a 0.3π maximum phase shift — limited by the $\mathcal{O}(1)$ linewidth cavity detuning produced at peak μLED intensity — was possible with energy densities below 10 fJ/μm^2 (corresponding to ∼100 fJ total energy for our chosen demagnification) and a minimum trigger duration $T_{\text{CMOS}} \approx 5$ ns. Shorter trigger pulses produce relatively constant-width pulses (due to the μLED fall time) with insufficient energy for high-contrast switching. Combined with the amplitude-dominant cross-polarization measurement, these μLED's time dynamics (approaching those of the cavity ringdown) explain the observed deviation in switching characteristics from Fig. 3f.

Confining visible pump pulses in space and time to the silicon free-carrier diffusion length (~ 1 μm) and lifetime ($\tau \approx 1$ ns), respectively, would minimize switching energy and maximize bandwidth. While either metric is achievable with existing μLED arrays [32, 53] and optimization to achieve both simultaneously is ongoing [54, 55], we demonstrated the expected performance enhancement with a pulsed visible ($\lambda = 515$ nm) laser. Fig. 6b shows that 3 dB power reflectivity changes and high-contrast phase modulation are feasible for 5 fJ pump pulses over a switching interval $T_{\text{switch}} \approx 1$ ns, thereby satisfying (C4). Free-carrier dispersion is the dominant switching mechanism for these isolated, ns-order switching events (Supplement Section A). While repeated switching over μs-order timescales leads to a slowly-varying thermo-optic detuning [56], various optical communications techniques (constant-duty line codes, for example [57]) can maintain average device temperature and resonant wavelength during high-speed free carrier modulation (Supplement Section A). To demonstrate this decoupling of switching mechanisms that enables continuous operation, we measured the normalized small-signal transfer function $T(\omega)$ between a harmonic pump power (produced by a network analyzer-driven amplitude electro-optic modulator) and the phase-locked homodyne response. When aligned to the thermally-detuned resonance, the results (Fig. 6c) match the expected second-order response $T(\omega) = 1/\{\left[1 + (\omega\tau)^2\right]\left[1 + (\omega/\pi\Gamma)^2\right]\}$ set by carrier- and cavity-lifetime-limited bandwidths. While satisfying (C2) therefore requires higher-Q resonators, the current regime of operation enables near-complete control over a larger bandwidth $\omega_s = 2\pi \times 135$ MHz $\approx 1/\tau$ without significantly degrading the carrier-lifetime-limited modulation bandwidth.

Combining this optimized switching with the space-bandwidth-limited vertical beaming of each resonator enables multimode programmable optics approaching the fundamental limits of spatiotemporal control. We currently probe the PhC-SLM in a wide-field, cross-polarized setup that produces amplitude-dominant Lorentzian reflection profiles $r(\Delta) \propto 1/(1 + j\Delta)$ regardless of the resonator coupling regime. For simplicity, we therefore conducted proof-of-concept demonstrations using the PhC-SLM as an array of high-speed binary amplitude modulators. In this modality, a nanosecond-class pulsed visible laser is passively fanned out to the desired devices. Devices targeted by pump light are detuned far from resonance ($\Delta \gg \Gamma$) and effectively extinguished, whereas unactuated cavities retain their high reflectivity at $\Delta \approx 0$.

We used pump-probe spectroscopy for wide-field imaging of these few-nanosecond switching events (Methods). Fig. 6e-f plots the resulting far-field intensity profiles $|E_r|^2$ for horizontal and vertical on-off gratings. For a 5 ns probe pulse width, the maximum near-field extinction of targeted cavities (7.4 dB and 9.8 dB for horizontal and vertical gratings, respectively) occurs within a ∼6 ns delay; i.e. just after the pump and probe pulses completely overlap. As expected, the input field is primarily scattered into first-order diffraction peaks within the (greater than 10°) 2D field-of-view of $S(\vec{k})$. The illustrated cross sectional beam profiles again agree with analytic results for a 80% filled linear array of uniform apertures (black dashed lines). For the horizontal grating Fig. 6e, the fit is scaled by a factor of ∼2 to account for the *increased* reflectivity of unactuated cavities during switching events, which we attribute to residual coupling between adjacent cavities. In both cases, the pattern diffraction efficiencies — measured as the fraction of integrated power within the outlined regions in Fig. 6 — $(\eta_x, \eta_y) = (0.22, 0.20)$ compare favorably to the efficiency of the fitted uniform aperture array. Even with amplitude-dominant modulation, these metrics exceed the efficiencies of previous resonator-based experiments due to our high-directivity PhC antenna array [35].

Summary and Outlook

These proof-of-concept experiments demonstrate near-complete spatiotemporal control of a narrow-band optical field filtered in space and time by an array of wavelength-scale, high-speed resonant modulators. While the general resonant architecture (Fig. 1c) is applicable to a range of microcavity geometries and modulation schemes, our combination of high-Q, vertically-coupled PhC cavities with efficient, all-optical free-carrier modulation achieves (C1-5) with an ultrahigh per-pixel spatiotemporal bandwidth $\nu \approx 5.6$ MHz·sr. This MHz-order modulation bandwidth per aperture-limited spatial mode corresponds to a more than ten-fold improvement over the 2D spatial light modulators reviewed in Fig 1b. Our wafer-scale fabrication and parallel trimming offer a direct route towards scaling this performance to spectrally-multiplexed, $\mathcal{O}(\text{cm}^2)$ apertures for a myriad of envisioned applications beyond the reach of current electronic systems (Methods), thus motivating the continued development of optical addressing and control techniques.

Acknowledgments

The authors thank the MITRE Quantum Moonshot Program, Flexcompute, Inc. for supporting FDTD simulations, the MIT.nano staff for fabrication assistance, and M. ElKabbash (MIT) for useful discussions. C.P. was supported by the Hertz Foundation Elizabeth and Stephen Fantone Family Fellowship. S.T.M. is funded by the Schmidt Postdoctoral Award and the Israeli Vatat Scholarship. Experiments were supported in part by Army Research Office grant W911NF-20-1-0084 (D.E.), supervised by M. Gerhold, the Engineering and Physical Sciences Research Council grants EP/M01326X/1 and EP/T00097X/1 (M.D., M.S.), and the Royal Academy of Engineering Research Chairs and Senior Research Fellowships (M.D., M.S.). This material is based on research sponsored by Air Force Research Laboratory under agreement number FA8650-21-2-1000. The U.S. Government is authorized to reproduce and distribute reprints for Governmental purposes notwithstanding any copyright notation thereon. The views and conclusions contained herein are those of the authors and should not be interpreted as necessarily representing the official policies or endorsements, either expressed or implied, of the United States Air Force, the Air Force Research Laboratory or the U.S. Government.

Author Contributions

C.P. and D.E. conceived the idea, developed the theory, and led the research. M.M. and C.P. developed the far-field optimization technique and designs. C.B. developed the optimized resonator detuning theory. C.P. conducted the experiments with assistance from I.C. (trimming experiments), S.T.M. (holography software), and A.G. (μLED measurements). J.J.M., M.D., and M.S. contributed the μLED arrays and guided the incoherent switching experiments. C.H. and J.W.B. fabricated the initial samples for evaluation prior to foundry process development by C.T., J.S.L., J.M., and G.L. S.P. assisted with wafer post-processing. M.F. coordinated and led the foundry fabrication with assistance from G.L. and D.C. C.P. wrote the manuscript with input from all authors.

Competing Interests

C.P. and D.E. are authors of US Patent 11,022,826 (All-optical spatial light modulators) and US Patent App. 16/876,477 (High-Speed Wavelength-Scale Spatial Light Modulators with Two-Dimensional Tunable Microcavity Arrays) which outline the all-optical control scheme and resonant architecture of the PhC-SLM developed here.

Main Text Figures

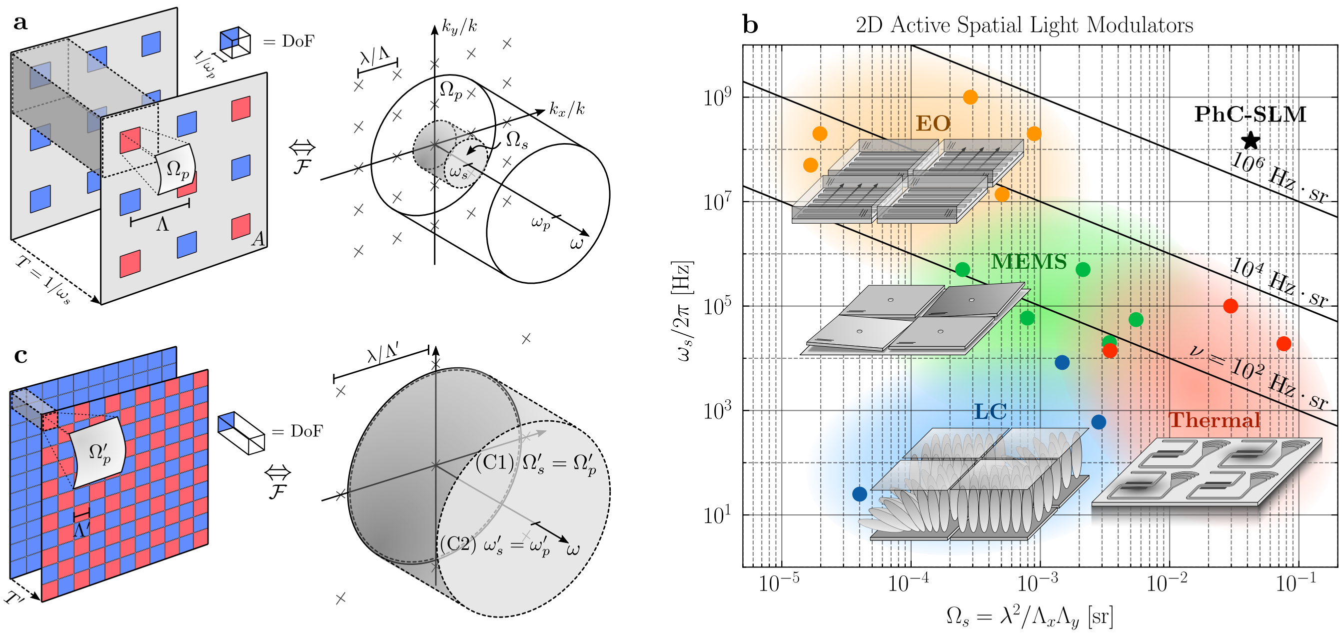

Figure 1: **Full degree-of-freedom (DoF) spatiotemporal optical programming.** Present-day SLMs (a) feature a 2D array of Λ-pitch pixels within an aperture area A. Each pixel radiates at wavenumber $k = 2\pi/\lambda$ into the solid angle Ω_p and can be switched (blue $\leftrightarrow$ red color change indicates a π phase change of the emitted field) over the timescale $T = 1/\omega_s$ (given a modulation bandwidth ω_s) with a large but slow fractional permittivity perturbation $\Delta\epsilon_p/\epsilon$ (e.g. liquid crystal rotation). The shaded volume indicates the smallest controllable near-field spatiotemporal mode. In the far-field (right), the corresponding shaded spatiotemporal bandwidth $\nu = \Omega_s\omega_s = (\lambda/\Lambda)^2\omega_s$ counts the controllable DoF per unit area and time in a single diffraction order. Trade-offs between ω_s and Ω_s in liquid crystal- (LC), thermal-, micro-electro-mechanical system- (MEMS), and electro-optic-driven (EO) SLMs (b; based on Table E1) limit $\nu \ll \Omega_p\omega_p$, the accessible pixel spatiotemporal bandwidth given the delay-limited bandwidth $\omega_p \sim ck\Delta\epsilon_p/\epsilon$. Spatiotemporal control is thus limited and scattering into undesired diffraction orders (grey $\times$s) reduces diffraction efficiency. Alternatively, a fully-filled array of wavelength-scale resonant apertures (c) emitting into the solid angle Ω'_p can enhance the effect of fast (modulation frequency ω'_s), low-energy perturbations $\Delta\epsilon'_p \ll \epsilon$ to simultaneously achieve space- and time-bandwidth limits (C1 and C2, respectively), yielding near-complete spatiotemporal control with $\nu' \approx \Omega'_p\omega'_p$.

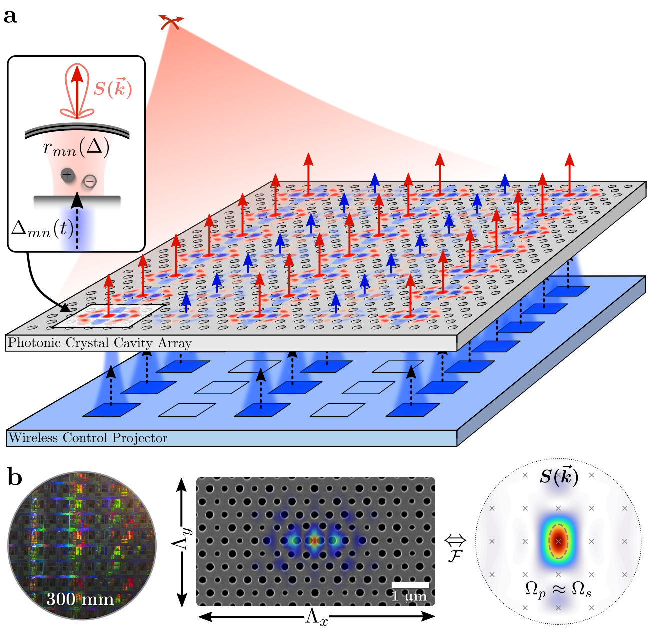

c

Criteria	Description	PhC-SLM
C1	Space-bandwidth limited (full fill)	$\Omega_s/\Omega_p \approx 1$
C2	Time/delay-bandwidth limited	$\omega_s/\omega_p > 0.1$
C3	Maximize spatiotemporal bandwidth	$\nu >$ MHz $\cdot$ sr
C4	fJ-order switching energy (E_{switch})	$E_{\text{switch}} \approx 5$ fJ
C5	Scalable foundry fabrication	300 mm wafer

Figure 2: **The photonic crystal spatial light modulator (PhC-SLM).** Complete spatiotemporal control is achieved by modulating an array of high-quality-factor ($Q > 10^5$), small-mode-volume ($V < 0.1\lambda^3$) silicon PhC cavities with a high-speed incoherent μLED array (a). Absorbed μLED pulses control the detuning Δ of resonant pixels via free carrier dispersion, which varies the amplitude and phase (illustrated by the length and color, respectively, of emission arrows at each cell) of the pixel's complex reflection coefficient $r(\Delta)$. Despite sub-wavelength near-field confinement (b, inset simulated mode profile overlaid on a SEM micrograph of an $L4/3$-type cavity [58]), each pixel is designed for directional ($\Omega_p \approx \Omega_s = \lambda^2/\Lambda_x\Lambda_y$) far-field scattering $S(\vec{k})$ into the zeroth diffraction order (marked by ×s) to satisfy (C1). Combining the reflection from each resonant "antenna" in a large-scale aperture fabricated via optimized 300 mm wafer-scale processing (b, inset photograph) enables near-ideal SLM performance per the design criteria (C1-5) (c).

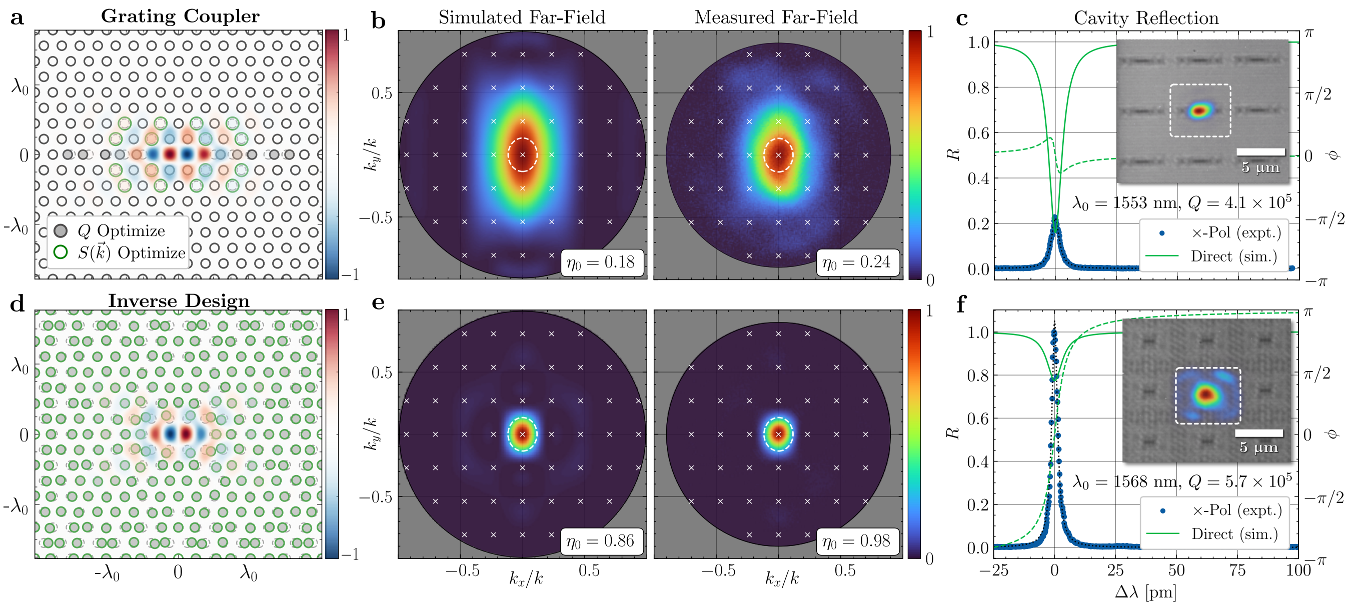

Figure 3: **Conventional (a-c) vs inverse-designed (d-f) PhC cavities.** (a) Superimposing a grating perturbation (green circles) on a Q-optimized $L3$ fundamental cavity mode (Fig. E1) improves vertical coupling at the expense of Q, yielding the simulated far-field intensity profile in (b, left) with $\eta_0 = 0.18$. Hole displacements and enlargements are magnified by 3× and 20×, respectively, for visualization. Our measured far-field profile (b, right) confirms the broad emission relative to the array field-of-view (dashed white line) Ω_s. This mismatch explains the low effective "fill factor" and poor coupling observed in our resonant imaging (c, inset) and near-field reflection spectra (c, blue), respectively. An input Gaussian beam (with waist matched to the pixel dimensions) is undercoupled and exhibits an amplitude-dominant power reflectivity $R = |r|^2$ modulation (c, solid green) with small phase variation $\Delta\phi$ (c, dashed green). Our inverse designed cavities (d) overcome these issues by optimizing *every* hole in the unit cell to vertically scatter cavity leakage for any target Q, producing "ideal" resonant SLM pixels satisfying (C1). Specifically, they support near-diffraction-limited emission (e) with $\eta_0 \sim 1$ due to fully-filled near-field resonant scattering (f, inset), a ∼5× experimental resonance contrast enhancement (f), and > 94% single-sided (i.e. assuming an ideal back-reflector as described in Supplement Section E) coupling to an input Gaussian beam for phase-dominant modulation (f, green).

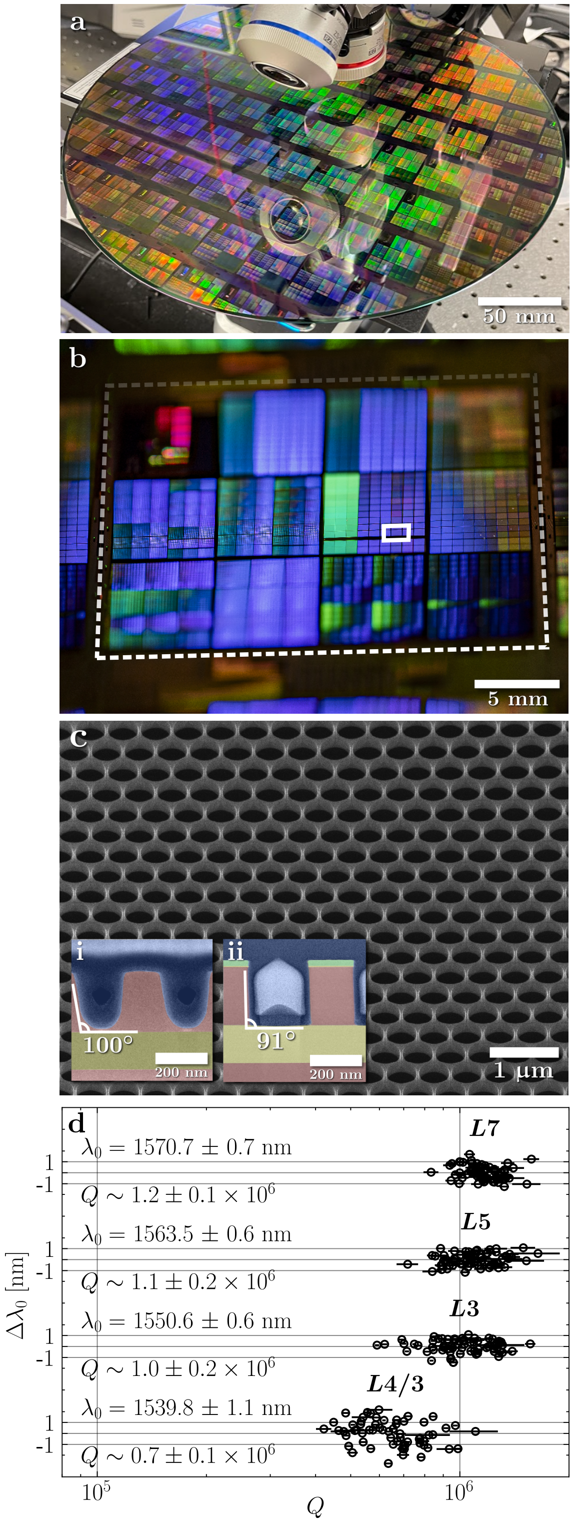

Figure 4: **Full-wafer photonic crystal fabrication in an optimized 300 mm foundry process.** A wafer (a) contains 64 complete reticles (b) each comprising millions of inverse designed PhC cavities. The before (i) and after (ii) false-color (blue: metal fill; red: silicon; yellow: silicon dioxide; green: etch mask) transmission electron microscope cross-sections show how process optimization enables high-quality PhC lattices (c) that support Lm-type cavity arrays with $\langle Q \rangle > 10^6$ and sub-nanometer wavelength standard deviation (d).

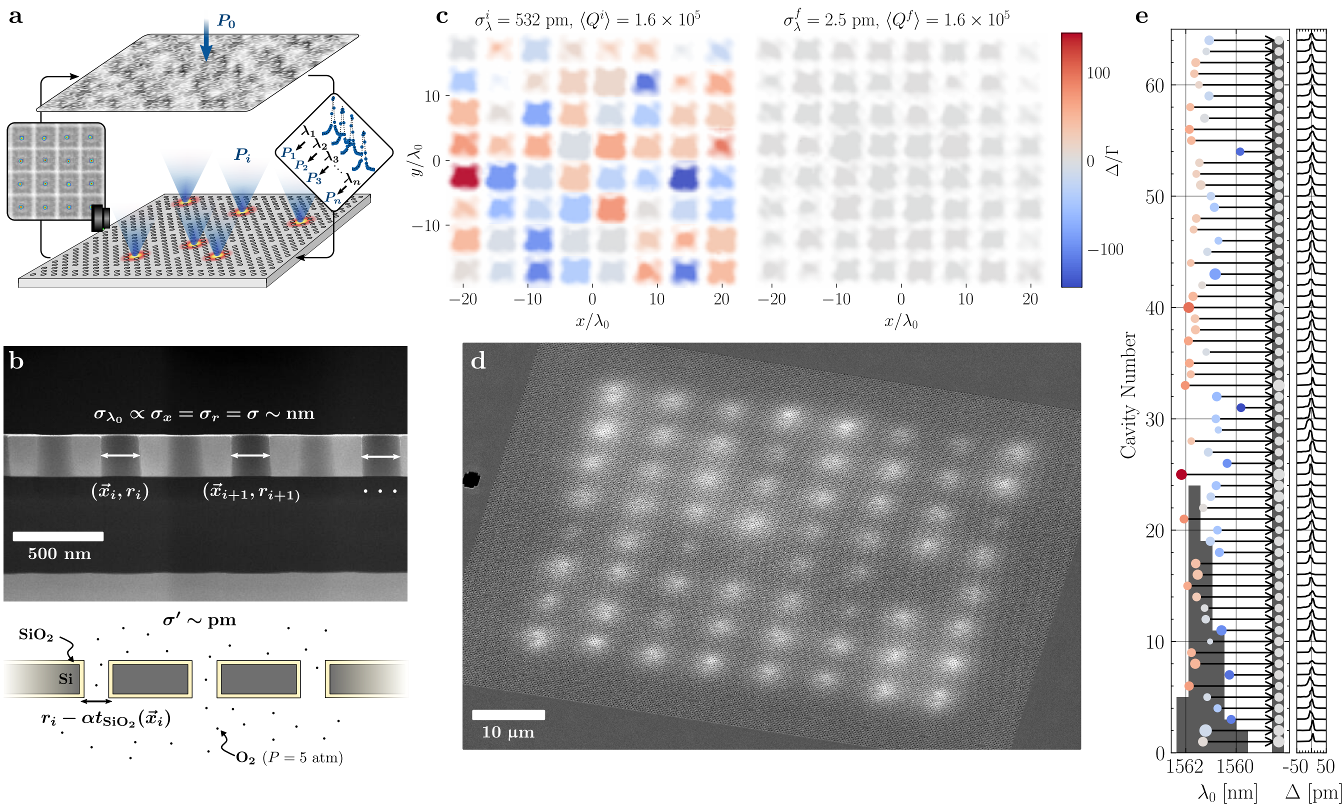

Figure 5: **Parallel, fully-automated, and low-loss microcavity trimming via structured laser oxidation.** In each iteration of the trimming loop (a), a weighted GS algorithm distributes a visible trimming laser with power P_0 to powers $\{P_i\}$ at desired cavities based on the measured resonant wavelength λ_i of each cavity. A few nm-thick layer of thermal oxide grows at each optical focus (photographed spots in the inset cavity array image), reducing the as-fabricated standard deviation in hole parameters $\sigma \sim$ nm (b) and permanently shifting the targeted resonances. The initial and final near-field hyperspectral reflection images (c, color-coded by each device's wavelength normalized detuning Δ/Γ) show the $> 100\times$ reduction in resonant-wavelength standard deviation to $\sigma_\lambda = 2.5$ pm without affecting the mean quality factor $Q > 10^5$. The effective dimensions of the final array (d) are thus homogenized to $\sigma' \sim$ pm length-scales by oxidation. Regions of local oxide growth in helium ion microscopy images of the trimmed PhC-SLM (d) appear as bright areas. The device summary (e) shows the wavelength shift, Q variation (quantified by dot area), and aligned reflection spectra of each device.

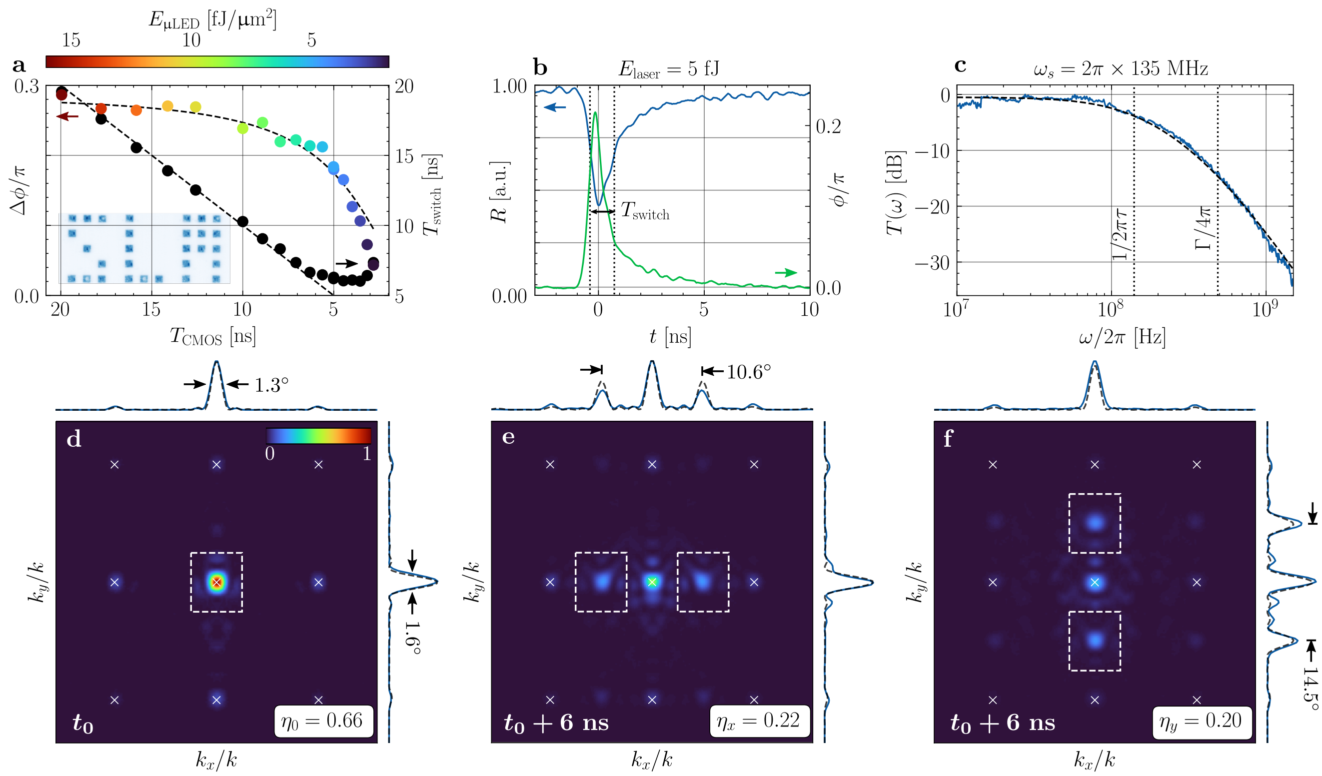

Figure 6: **Nanosecond switching (a-c) and spatial light modulation (d-f).** (a) Peak phase shift $\Delta\phi$ and half-maximum switching interval T_{switch} produced by pulses from a CMOS-integrated μLED array imaged onto the cavity array (inset: cavities illuminated to form the letters 'S', 'L', and 'M') as a function of trigger duration T_{CMOS} and pulse energy density $E_{\mu\mathrm{LED}}$. (b) Complex reflectivity ($r = \sqrt{R}e^{j\phi}$) modulation with femtojoule-order pulse energies E_{laser} from a focused visible laser. (c) Output probe to input visible (pump) power transfer function $T(\omega)$ fit to a second-order response function, yielding $\omega_s = 2\pi \times 135$ MHz limited by the free carrier lifetime $\tau \approx 1.1$ ns and cavity bandwidth $\Gamma \approx 1$ GHz. (d) Far-field intensity profile, half-maximum beam widths, and zero-order diffraction efficiency η_0 (integrated within the dashed white box) of the trimmed array at time t_0 with horizontal and vertical cross-sectional profiles (blue traces) compared to those of an 8×8 array of planar apertures with 80% linear fill (black, dashed). (e/f) Analogous results for the switched array with an optically-patterned horizontal (vertical) amplitude grating at the maximum extinction time $t_0 + 6$ ns, producing $\pm1^{\mathrm{st}}$-order diffraction peaks over a 10.6° (14.5°) field-of-view and diffraction efficiency $\eta_x = 0.22$ ($\eta_y = 0.20$).

References

[1] Gardner, J. P. *et al.* The James Webb Space Telescope. *Space Science Reviews* **123**, 485–606 (2006).

[2] Packer, A. M., Roska, B. & Häusser, M. Targeting neurons and photons for optogenetics. *Nature neuroscience* **16**, 805–815 (2013).

[3] Demas, J. *et al.* High-speed, cortex-wide volumetric recording of neuroactivity at cellular resolution using light beads microscopy. *Nature Methods* **18**, 1103–1111 (2021).

[4] Hamerly, R., Bernstein, L., Sludds, A., Soljačić, M. & Englund, D. Large-scale optical neural networks based on photoelectric multiplication. *Physical Review X* **9**, 021032 (2019).

[5] Bogaerts, W. *et al.* Programmable photonic circuits. *Nature* **586**, 207–216 (2020).

[6] Wetzstein, G. *et al.* Inference in artificial intelligence with deep optics and photonics. *Nature* **588**, 39–47 (2020).

[7] Kok, P. *et al.* Linear optical quantum computing with photonic qubits. *Reviews of modern physics* **79**, 135 (2007).

[8] Ebadi, S. *et al.* Quantum phases of matter on a 256-atom programmable quantum simulator. *Nature* **595**, 227–232 (2021).

[9] Shaltout, A. M., Shalaev, V. M. & Brongersma, M. L. Spatiotemporal light control with active metasurfaces. *Science* **364**, eaat3100 (2019).

[10] Li, S.-Q. *et al.* Phase-only transmissive spatial light modulator based on tunable dielectric metasurface. *Science* **364**, 1087–1090 (2019).

[11] Zhang, X., Kwon, K., Henriksson, J., Luo, J. & Wu, M. C. A large-scale microelectromechanical-systems-based silicon photonics LiDAR. *Nature* **603**, 253–258 (2022).

[12] Sun, J., Timurdogan, E., Yaacobi, A., Hosseini, E. S. & Watts, M. R. Large-scale nanophotonic phased array. *Nature* **493**, 195–199 (2013).

[13] Rogers, C. *et al.* A universal 3D imaging sensor on a silicon photonics platform. *Nature* **590**, 256–261 (2021).

[14] Wu, P. C. *et al.* Dynamic beam steering with all-dielectric electro-optic III-V multiple-quantum-well metasurfaces. *Nature communications* **10**, 1–9 (2019).

[15] Zhang, Y. *et al.* Electrically reconfigurable non-volatile metasurface using low-loss optical phase-change material. *Nature Nanotechnology* **16**, 661–666 (2021).

[16] Park, J. *et al.* All-solid-state spatial light modulator with independent phase and amplitude control for three-dimensional LiDAR applications. *Nature nanotechnology* **16**, 69–76 (2021).

[17] Wang, Y. *et al.* Electrical tuning of phase-change antennas and metasurfaces. *Nature Nanotechnology* **16**, 667–672 (2021).

[18] Gabor, D. Light and information. In *Progress in optics*, vol. 1, 109–153 (Elsevier, 1961).

[19] Miller, D. A. Fundamental limit to linear one-dimensional slow light structures. *Physical review letters* **99**, 203903 (2007).

[20] Miller, D. A. Attojoule optoelectronics for low-energy information processing and communications. *Journal of Lightwave Technology* **35**, 346–396 (2017).

[21] Panuski, C. L. & Englund, D. R. All-optical spatial light modulators (2021). US Patent 11,022,826.

[22] Soref, R. A. & Bennett, B. R. Electrooptical effects in silicon. *IEEE journal of quantum electronics* **23**, 123–129 (1987).

[23] Tanabe, T., Taniyama, H. & Notomi, M. Carrier diffusion and recombination in photonic crystal nanocavity optical switches. *Journal of Lightwave Technology* **26**, 1396–1403 (2008).

[24] Panuski, C., Pant, M., Heuck, M., Hamerly, R. & Englund, D. Single photon detection by cavity-assisted all-optical gain. *Physical Review B* **99**, 205303 (2019).

[25] Huang, Y., Hsiang, E.-L., Deng, M.-Y. & Wu, S.-T. Mini-LED, Micro-LED and OLED displays: Present status and future perspectives. *Light: Science & Applications* **9**, 1–16 (2020).

[26] Lin, J. & Jiang, H. Development of microLED. *Applied Physics Letters* **116**, 100502 (2020).

[27] Templier, F. *et al.* High-resolution active-matrix 10-um pixel-pitch GaN LED microdisplays for augmented reality applications. In *Advances in Display Technologies VIII*, vol. 10556, 105560I (International Society for Optics and Photonics, 2018).

[28] Chen, C.-J., Chen, H.-C., Liao, J.-H., Yu, C.-J. & Wu, M.-C. Fabrication and characterization of active-matrix 960×540 blue GaN-based micro-LED display. *IEEE Journal of Quantum Electronics* **55**, 1–6 (2019).

[29] Herrnsdorf, J. *et al.* Active-matrix GaN micro light-emitting diode display with unprecedented brightness. *IEEE Transactions on Electron Devices* **62**, 1918–1925 (2015).

[30] Ferreira, R. X. G. *et al.* High bandwidth GaN-based micro-LEDs for multi-Gb/s visible light communications. *IEEE Photonics Technology Letters* **28**, 2023–2026 (2016).

[31] Cai, Y. *et al.* Direct epitaxial approach to achieve a monolithic on-chip integration of a HEMT and a single micro-LED with a high-modulation bandwidth. *ACS applied electronic materials* **3**, 445–450 (2021).

[32] Park, J. *et al.* Electrically driven mid-submicrometre pixelation of ingan micro-light-emitting diode displays for augmented-reality glasses. *Nature Photonics* **15**, 449–455 (2021).

[33] Hassan, N. B. *et al.* Ultra-high frame rate digital light projector using chipscale LED-on-CMOS technology. *arXiv preprint arXiv:2111.13586* (2021).

[34] Miller, D. A. Optical interconnects to electronic chips. *Applied optics* **49**, F59–F70 (2010).

[35] Horie, Y., Arbabi, A., Arbabi, E., Kamali, S. M. & Faraon, A. High-speed, phase-dominant spatial light modulation with silicon-based active resonant antennas. *Acs Photonics* **5**, 1711–1717 (2017).

[36] Peng, C., Hamerly, R., Soltani, M. & Englund, D. R. Design of high-speed phase-only spatial light modulators with two-dimensional tunable microcavity arrays. *Optics express* **27**, 30669–30680 (2019).

[37] Lee, H. *et al.* Local tuning of photonic crystal nanocavity modes by laser-assisted oxidation. *Applied Physics Letters* **95**, 191109 (2009).

[38] Chen, C. J. *et al.* Selective tuning of high-Q silicon photonic crystal nanocavities via laser-assisted local oxidation. *Optics express* **19**, 12480–12489 (2011).

[39] Nozaki, K. *et al.* Sub-femtojoule all-optical switching using a photonic-crystal nanocavity. *Nature Photonics* **4**, 477–483 (2010).

[40] Tran, N.-V.-Q., Combrié, S. & De Rossi, A. Directive emission from high-Q photonic crystal cavities through band folding. *Physical Review B* **79**, 041101 (2009).

[41] Tran, N.-V.-Q., Combrié, S., Colman, P., De Rossi, A. & Mei, T. Vertical high emission in photonic crystal nanocavities by band-folding design. *Physical Review B* **82**, 075120 (2010).

[42] Portalupi, S. L. *et al.* Planar photonic crystal cavities with far-field optimization for high coupling efficiency and quality factor. *Optics express* **18**, 16064–16073 (2010).

[43] Qiu, C., Chen, J., Xia, Y. & Xu, Q. Active dielectric antenna on chip for spatial light modulation. *Scientific reports* **2**, 1–7 (2012).

[44] Hansen, R. C. Fundamental limitations in antennas. *Proceedings of the IEEE* **69**, 170–182 (1981).

[45] Fahrenkopf, N. M. *et al.* The AIM Photonics MPW: A highly accessible cutting edge technology for rapid prototyping of photonic integrated circuits. *IEEE Journal of Selected Topics in Quantum Electronics* **25**, 1–6 (2019).

[46] Asano, T., Song, B.-S. & Noda, S. Analysis of the experimental Q factors (∼1 million) of photonic crystal nanocavities. *Optics express* **14**, 1996–2002 (2006).

[47] Kim, S.-H., Kim, S.-K. & Lee, Y.-H. Vertical beaming of wavelength-scale photonic crystal resonators. *Physical Review B* **73**, 235117 (2006).

[48] Sekoguchi, H., Takahashi, Y., Asano, T. & Noda, S. Photonic crystal nanocavity with a Q-factor of ∼9 million. *Optics Express* **22**, 916–924 (2014).

[49] Taguchi, Y., Takahashi, Y., Sato, Y., Asano, T. & Noda, S. Statistical studies of photonic heterostructure nanocavities with an average Q factor of three million. *Optics express* **19**, 11916–11921 (2011).

[50] Minkov, M., Dharanipathy, U. P., Houdré, R. & Savona, V. Statistics of the disorder-induced losses of high-Q photonic crystal cavities. *Optics express* **21**, 28233–28245 (2013).
[51] Haus, H. A. *Waves and fields in optoelectronics*. Prentice-Hall series in solid state physical electronics (Prentice-Hall, Englewood Cliffs, NJ, 1984).
[52] Zhang, S. *et al.* 1.5 Gbit/s multi-channel visible light communications using CMOS-controlled GaN-based LEDs. *Journal of lightwave technology* **31**, 1211–1216 (2013).
[53] McKendry, J. J. *et al.* Individually addressable alingan microled arrays with cmos control and subnanosecond output pulses. *IEEE Photonics Technology Letters* **21**, 811–813 (2009).
[54] Lan, H.-Y. *et al.* High-speed integrated micro-led array for visible light communication. *Optics letters* **45**, 2203–2206 (2020).
[55] Pandey, A. & Mi, Z. III-Nitride nanostructures for high efficiency micro-LEDs and ultraviolet optoelectronics. *IEEE Journal of Quantum Electronics* (2022).
[56] Barclay, P. E., Srinivasan, K. & Painter, O. Nonlinear response of silicon photonic crystal microresonators excited via an integrated waveguide and fiber taper. *Optics express* **13**, 801–820 (2005).
[57] Winzer, P. J. & Essiambre, R.-J. Advanced modulation formats for high-capacity optical transport networks. *Journal of Lightwave Technology* **24**, 4711–4728 (2006).
[58] Minkov, M., Savona, V. & Gerace, D. Photonic crystal slab cavity simultaneously optimized for ultra-high Q/V and vertical radiation coupling. *Applied Physics Letters* **111**, 131104 (2017).
[59] Minkov, M. & Savona, V. Automated optimization of photonic crystal slab cavities. *Scientific reports* **4**, 1–8 (2014).

Methods

Comparison to Previous 2D SLMs

In general, commercial devices approximate design criterion (C1) without achieving (C2). Specifically, they offer excellent near-field fill-factor across megapixel-scale apertures but use large $\mathcal{O}(\epsilon)$, slow index perturbations. Liquid crystal SLMs, for example, are limited to $\omega_s \sim 2\pi \times 10^3$ Hz $\ll \omega_p$ by the slow rotation of viscous, anisotropic molecules that modulate the medium's phase delay [60, 61]. Digital micromirror-based SLMs offer moderately faster ($\sim 10^5$ Hz) binary amplitude modulation by displacing a mechanical reflector, but at the expense of diffraction efficiency [62]. Mechanical phase shifters [63–67] improve this efficiency but still require design trade-offs between pixel size and response time.

Recent research has focused on surmounting the speed limitations of commercial SLMs with integrated photonic phased arrays [12, 13, 69, 70] and active metasurfaces comprised of thermally [15, 17, 72], mechanically [66, 75], or electrically [14, 16, 76, 79, 80] actuated elements. These devices, however, do not satisfy (C1) (Table E1). Silicon photonics in particular has attracted significant interest due to its fabrication scalability; however, the combination of standard routing waveguides, high-power ($\sim$ mW/π phase shift) thermal phase shifters, and vertical grating couplers in each pixel reduces the fill-factor of emitters, yielding $\Omega_p \gg \Omega_s$ [12]. Scattering into the numerous diffraction orders within Ω_p then reduces the achievable zero-order and overall diffraction efficiencies (η_0 and η, respectively). For this reason, η_0 is a useful measure of near-field fill.

Various workarounds, including 1D phased arrays with transverse wavelength tunability [69, 81, 82], sparse antenna arrays [83], and switched arrays [11, 84] improve steering performance but restrict the spatiotemporal basis (i.e. limit F). Alternative nanophotonics-based approaches, often limited to 1D modulation, have their drawbacks as well: phase change materials [15, 17, 72] have slow crystallization rates and large switching energies, while electro-optic devices [16, 76, 79, 80, 86–88], to date, have primarily relied on large-area grating-based resonators to achieve appreciable modulation.

Table E1 compares the PhC-SLM demonstrated here to these other actively-controlled, 2D SLMs (Fig. 1b). Wavelength-steered devices and switch arrays are omitted to restrict focus to the typical SLM architectures in Fig. 1. Notably, while beamsteering with PhC waveguides [84, 89, 90] and laser arrays [91] has recently been demonstrated, our device is the first (to our knowledge) to feature simultaneous emission from a 2D array of individually controllable PhC pixels.

Inverse-Designed Photonic Crystal Antennas

Typical photonic crystal cavity designs — the $L3$ cavity in Fig. E1a, for example [59] — are designed to maximize Q by cancelling radiative leakage, yielding a broad far-field emission pattern (Fig. E1b, background) that violates (C1) and limits the zero-order diffraction efficiency (to $\eta_0 \approx 0.04$ in this case). The result is poor beamforming performance as exemplified by the distorted, low-efficiency far-field pattern emitted by a 64×64 cavity array with optimized detunings (derived with the algorithm in Supplement Section D) to match a target far-field image (MIT logo).

Alternatively, our inverse-design strategy (Fig. E1b) combines semi-analytic guided mode expansion (GME) simulations with efficient gradient-based optimization via automatic differentiation to enable high-quality beamforming with vertically-coupled, high-Q, and small-mode-volume photonic crystal microcavities. In each optimization step, GME (implemented with the open-source package `Legume` [92]) approximates the cavity eigenmode and radiative loss rates $c_{mn}^{(i)}$ at each of the array's reciprocal lattice vectors (i.e. diffraction orders) offset by the Bloch periodic boundary conditions $\vec{k}_i$ [93]. These coupling coefficients coarsely sample the cavity's approximate far-field emission. Scanning $\vec{k}_i$ over the irreducible Brillouin zone of the rectangular cavity array improves the sampling resolution, and an overall Q can be estimated by averaging the total loss rates $\Gamma^{(i)} = \sum_{mn} c_{mn}^{(i)}$ in each simulation. Reverse-mode automatic differentiation then allows us to efficiently optimize an objective function

$$f = \frac{1}{N} \sum_{i=1}^{N} \frac{c_{00}^{(i)}}{\Gamma^{(i)}} \arctan\left(\frac{Q}{Q_0}\right) |E_0|^2 \tag{3}$$

targeting three main goals: 1) increase Q to a design value Q_0; 2) force the associated radiative loss into the array's zeroth diffraction order for efficient vertical coupling; and 3) minimize V by maximizing $|E_0|$, the electric-field magnitude at the center of the unit cell. Supplement Section B further describes this technique in comparison to the existing grating coupler technique introduced in Sec. 1.

The resulting designs support high-efficiency free-space coupling (Supplement Section C) to photonic crystal microcavities with near-unity zero-order diffraction efficiency. Combined, these features enable high-quality microcavity-based beamforming as evidenced by the simulated hologram in Fig. E1d: an array of optimally detuned, inverse-designed cavities forms a clear far-field image with a several order-of-magnitude improvement in overall diffraction efficiency ($\eta = 0.83$) over existing designs.

Measurement Setups and Techniques

Fig. E2 schematically illustrates the major components of our experimental setup. Here, we describe the design and function of each sub-assembly.

Near-Field Characterization

The wide-field, cross-polarized microscope in Fig. E2(a) allows us to simultaneously measure the reflection from every cavity within a camera's field-of-view. A visible illumination path (not illustrated) is joined with collimated infrared light from a tunable laser with a dichroic mirror and focused onto the back-focal-plane (BFP) of an objective by lens L1. The angle-of-incidence and spot size of the infrared beam on the sample are therefore controlled by translating L1 and varying the collimated beam diameter, respectively. In our typical wide-field configuration, a 7.2 mm beam diameter focused to the center of a 40× objective's BFP yields a ∼150 µm waist-diameter, vertically-incident field that quasi-uniformly illuminates 10×10 PhC cavity arrays.

By orienting the input polarization at a 45° angle relative to the dominant cavity polarization axis (with a half-wave plate or by physically rotating the sample), light coupled into and reflected by the PhC cavity is polarization rotated and can be isolated from direct, specular reflections with a polarizing beamsplitter. A kHz-rate free-running, dual-band (visible and infrared) camera images this cross-polarized reflection signal through the tube lens L3. For each frame collected during a laser sweep, the wavelength is interpolated from the recorded camera and laser output triggers and each cavity's reflection is integrated over a fraction of pixels within its imaged unit cell boundary. We use the resulting high-contrast reflection spectra (across all devices within the field-of-view) to characterize device performance and monitor the cavity trimming process.

The sample mount below the objective (OL) is temperature stabilized to within 10 mK with a Peltier plate and feedback controller. For trimming experiments, the sample is placed in a high-pressure oxygen environment within a custom chamber offering in-situ optical access through a glass window.

Calibrated Far-Field Measurement

Inserting a lens (L2) in the collection path one focal length from the objective BFP allows us to measure the far-field profile $S(\vec{k})$ of individual or multiple cavities using the same setup. We position an iris at the intermediate image plane — located with a removable lens (not shown) placed before L3 — to spatially filter the emission from desired devices. We also calibrate the BFP scale using a reflective reference grating with known pitch. Due to the cross-polarized configuration, only a single polarization $\tilde{S}(\vec{k})\big|_\theta$ is imaged for any cavity-input polarization angle difference θ. The complete cavity emission profile

$$S(\vec{k}) = \tilde{S}(\vec{k})\big|_\theta + \tilde{S}(\vec{k})\big|_{\theta\pm\pi/2} \tag{4}$$

can therefore be reconstructed by sequentially imaging both polarizations as in Figs. E3a-c for $\theta = 45°$. For maximum accuracy, we used this technique for the experimental results in Fig. 3.

Alternatively, the specific choice $\theta = 45°$ allows $S(\vec{k})$ to be reconstructed from a single measurement. Due to mirror symmetry about the cavity's principal polarization axis $\hat{y}$, Fig. E3a-b show that $\hat{\sigma}_{\hat{y}}\{\tilde{S}(\vec{k})\big|_{\pm45°}\} = \tilde{S}(\vec{k})\big|_{\mp45°}$ for the reflection operator $\hat{\sigma}$. This alternative reconstruction

$$S(\vec{k}) = [1 + \hat{\sigma}_{\hat{y}}]\, S(\vec{k})\big|_{\pm45°} \tag{5}$$

is demonstrated experimentally in Fig. 3d, yielding excellent agreement with Fig. 3c.

This technique simplifies high-throughput far-field measurements across cavity arrays. In Fig. E4, for example, we used this approach to demonstrate the far-field uniformity characteristic of inverse-designed and grating coupled $L3$ cavity arrays. Averaged across the 8×8 arrays, the former offers a $\sim3\times$ improvement in zero-order diffraction and aperture efficiencies ($\langle\eta_0\rangle = 0.86$, $\langle\eta_a\rangle = 0.99$).

Pump-Probe Spectroscopy

Widefield, time-resolved near- and far-field measurements can also be collected using the setup in Fig. E2a via pump-probe spectroscopy. For these measurments, short infrared probe pulses were carved with a electro-optic amplitude modulator (EOM) DC biased to an intensity null and variably delayed to coincide with the arrival of visible pump light at the PhC membrane, thereby gating probe field transmission to the IR camera. We then measured the near- and far-field reflection as a function of the probe delay to reconstruct switching events with sub-nanosecond resolution. The minimum probe pulse width (~5ns) used to collect the data in Fig. 6e-f was limited by the requirement for high imaging contrast between probe pulses and leakage (due to the imperfect probe modulator extinction) given the instrument-limited trigger repetition rate (~MHz) and camera integration time.

Homodyne Measurement

The shot-noise-limited balanced homodyne detection setup in Fig. E2c enables complex reflection coefficient measurements with greater than >3 dB shot-noise clearance below 1 GHz [94]. Signal light reflected from the cavity combines with a path-length-matched (to within ~mm based on time-delay measurements with a picosecond-class pulsed laser) local oscillator (LO), and both signals are coupled into a balanced detector using anti-reflection coated fibers. The in-phase ($I(t)$) and quadrature ($Q(t)$) components of the cavity reflection were sequentially measured by locking to the first and second harmonics of the balanced output in the presence of a piezo-driven LO phase dither. The resonant, cross-polarized cavity reflection R and phase shift ϕ are then reconstructed as

$$R = \frac{[V_p - I(t)]^2 + Q^2(t)}{V_p^2} \qquad\qquad \phi = \arctan\frac{Q(t)}{V_p - I(t)} \tag{6}$$

by normalizing to the measured peak voltage swing V_p of the interference signal.

Parallel Cavity Trimming

A liquid crystal on silicon (LCOS) SLM (Fig. E2c) actively distributes a high-power, continuous-wave visible laser to target devices during the cavity trimming procedure. The input laser was tunably attenuated with a motorized half-wave plate (preceding a PBS) and subsequently expanded to overfill the LCOS aperture. The LCOS SLM was re-imaged onto the objective BFP (as confirmed by imaging with L2 in place) using two lenses (L4, L5) with focal lengths chosen to optimally match the imaged SLM and objective pupil dimensions. Phase retrieval-computed holograms then evenly distribute power to an array of focused spots on the sample (Supplement Section F) when the mechanical, flip mirror shutter is opened.

µLED Imaging

The collection optics in Fig. E2d maximize the intensity of a µLED array projected onto the PhC membrane within the constraints dictated by the constant radiance theorem of incoherent imaging. Assuming a Lambertian emission profile, geometric optics gives the collection efficiency $\eta_c = \alpha_c^2$ for an objective lens (CL) with numerical aperture α_c focused on the µLED array. The projection efficiency η_p through the projection objective (OL, with numerical aperture α_p) depends on the relative pupil sizes of both objectives and can be similarly approximated from geometric optics. The resulting intensity enhancement $\zeta = \eta_c\eta_p/M^2$ between the source and image (with magnification M) reaches a maximum $\zeta_{\max} = \frac{1}{M^2+(1-\alpha_p^2)/\alpha_p^2}$ when the CL-collimated light overfills the back aperture of OL. The resulting design criteria,

$$\alpha_c > \sqrt{\frac{M^2\alpha_p^2}{(M^2-1)\alpha_p^2+1}}, \tag{7}$$

is achieved for our imaging setup with $\alpha_c = 0.25$, $\alpha_p = 0.95$, and $M \approx 1/30$. After CL, The overall magnification and rotation are fine-tuned with a variable beam expander and Dove prism, respectively.

Holographic Trimming

In each iteration of the automated trimming loop (Fig. 5a), the resonant wavelengths $\{\lambda_i\}$ are measured and a subset T containing N devices is selected to maximize the total trimming distance $N(\min_T\{\lambda_i\} - \lambda_t)$ to a target wavelength λ_t. Each cavity in T is then targeted by a visible laser distributed by the liquid crystal SLM setup (Fig. E2c). To generate the required phase masks, we developed an open-source, GPU-accelerated experimental holography software package that implements fixed-phase, weighted Gerchberg-Saxton (GS) phase retrieval algorithms. Using camera feedback, the algorithm can generate thousands of near-diffraction-limited foci with $\sim$1% peak-to-peak power uniformity and single-camera-pixel-order location accuracy within a few iterations (Supplement Section F).

The holographically-targeted pixels are then laser-heated with a computed exposure power and duration (based on the current trimming rates, resonance locations, and other array characteristics) to grow thermal oxide at the membrane surface. For thin oxide layers, the consumption of silicon during the reaction with ambient oxygen permanently blueshifts the cavity resonance in proportion to the oxide thickness $t_{\mathrm{SiO_2}}$ (Fig. 5b) [38]. Per the Deal-Grove model, the rate-limiting diffusion of oxygen through the grown oxide accelerates with increasing oxygen pressure — a well-known technique in microelectronics fabrication [96]. We therefore oxidize our samples in pure oxygen with partial pressure $P_{\mathrm{O_2}} = 5$ bar, enabling $\mathrm{d}\lambda_0/\mathrm{d}t \approx 0.1$ nm/s resonance trimming rates over $\Delta\lambda_0 > 20$ nm wavelength ranges. After each trimming exposure, we remeasure the resonance statistics and recycle the loop until all devices are aligned within a set tolerance about λ_t. The trimming algorithm also accounts for long-term moisture adsorption to the membrane surface, thermal cross-talk, and trimming rate variations.

Fig. 5 schematically outlines this trimming procedure. The main loop consists of device selection, hologram setup, parallel laser oxidation, and resting intervals. The algorithm monitors two resonant wavelengths: the instantaneous wavelength λ_i and the steady-state wavelength λ_0. Initially $\lambda_i = \lambda_0$; however, focusing high-power (∼10 mW) visible light onto the cavity (as required to sufficiently heat the PhC membrane for thermal oxidation) causes a temporary blueshift $\Delta\lambda_0$ due to the desorption of moisture attached to hydrophilic hydroxyl surface terminations. For any target rest wavelength λ_t, we therefore trim devices to an instantaneous wavelength $\lambda_i = \lambda_t - \Delta\lambda_0$ that relaxes over $\mathcal{O}$(minute) timescales to $\lambda_i = \lambda_0 = \lambda_t$ as moisture re-adsorbs to the surface. In practice, the stability and estimation of the "overtune" $\Delta\lambda_0$ limit the uniformity and scale of the trimming process, respectively.

After initializing the cavity locations, scanning the device resonances, and calibrating the SLM (Section F), a spot array targeting every cavity (e.g. Fig. E6) is projected on the membrane for a short (few second) duration. Monitoring the resonances at fixed intervals $\Delta t \approx 10$ s until λ_i stabilizes to the rest wavelength λ_0 gives an initial estimate $\Delta\lambda_0 = \lambda_0 - \min\{\lambda_i\}$ for the overtune parameter of each cavity. We also update the target wavelength $\lambda_t = \min\{\lambda_0\}$ and rest wavelengths before continuing the trimming procedure. To update $\Delta\lambda_0$, we periodically conduct this same "rest loop" when λ_0 of each cavity is below an algorithmically chosen "checkpoint" wavelength λ_{rest}.

As described in Section 3, a subset of N cavities is then selected to maximize the total possible trimming distance to λ_t. The number of targeted cavities neighboring each untargeted cavity is also limited to reduce crosstalk. A spot array is then formed to evenly distribute the trimming laser to the selected devices. After confirming that the location accuracy and power uniformity of the array are within tolerance, we alternate exposure and readout intervals to grow thermal oxide with in situ monitoring. The laser power is progressively increased to reach a desired, wavelength-uniformity-dependent trimming rate. As evidenced by Fig. A8, the rate is relatively power-independent until reaching a threshold power. We detect and save these threshold powers for use when selecting the initial exposure power in each trimming loop.

The trimming sub-loop continues until the estimated λ_0 of any targeted cavity crosses λ_t. New cavities are then selected, targeted, and trimmed until a rest period is triggered. When the peak-to-peak wavelength uniformity at the end of a rest period is below the user-defined tolerance λ_{tol}, the process is terminated. Table E2 compares the demonstrated performance compared to other arrayed microcavity trimming techniques.

Envisioned Applications

The PhC-SLM opens the door to a number of applications and opportunities including: *high-definition, high-frame-rate holographic displays* by the integration of a back-reflector (see Appendices C-E) for one-sided, phase-only, and full-DoF spatiotemporal modulation; *compact device integration* via direct transfer printing of our cavity arrays onto a high-bandwidth µLED array [97]; *three-dimensional optical addressing and imaging* by combining on-demand µLED control with statically trimmed detuning profiles that continuously steer pre-programmed patterns [98]; *large-scale programmable unitary transformations* for universal linear optics processors [5] enabled by overcoupled PhC reflectors; *focal plane array sensors* for high-spatial-resolution readout of refractive index perturbations in imaging applications from endoscopy to bolometry and quantum-limited superresolution [100–102]; *optical neural network acceleration* via low-power, high-density unitary transformation of free-space optical inputs [4, 6]; and *high-speed adaptive optics* enabling free-space compressive sensing, deep-brain neural stimulation, and real-time scattering matrix inversion in complex media [105, 106]. Moreover, whereas we have so far considered only mode transformations, the PhC-SLM's high-Q/V resonant enhancement suggests the possibility of programming the quantum optical excitations/fields of these modes for applications ranging from multimode squeezed light generation [107], to multiplexed single photon sources for linear optics quantum computing [7, 109] or deterministic photonic logic [110, 111].

Data Availability

The main data supporting the findings of this study are available within the Article and its Supplementary Information. Additional data are available from the corresponding authors upon reasonable request.

Code Availability

The SLM control and holography software developed for this study is available online via the `slmsuite` open source package. All other algorithms are documented within the Article and its Supplementary Information.

Methods References

[60] Heilmeier, G. H., Zanoni, L. A. & Barton, L. A. Dynamic scattering: A new electrooptic effect in certain classes of nematic liquid crystals. *Proceedings of the IEEE* **56**, 1162–1171 (1968).

[61] Zhang, Z., You, Z. & Chu, D. Fundamentals of phase-only liquid crystal on silicon (LCOS) devices. *Light: Science & Applications* **3**, e213–e213 (2014).

[62] Ren, Y.-X., Lu, R.-D. & Gong, L. Tailoring light with a digital micromirror device. *Annalen der physik* **527**, 447–470 (2015).

[63] Hornbeck, L. J. 128× 128 deformable mirror device. *IEEE Transactions on Electron Devices* **30**, 539–545 (1983).

[64] Greenlee, C. *et al.* Electro-optic polymer spatial light modulator based on a fabry–perot interferometer configuration. *Optics express* **19**, 12750–12758 (2011).

[65] Yang, W. *et al.* High speed optical phased array using high contrast grating all-pass filters. *Optics express* **22**, 20038–20044 (2014).

[66] Wang, Y. *et al.* 2D broadband beamsteering with large-scale MEMS optical phased array. *Optica* **6**, 557–562 (2019).

[67] Tzang, O. *et al.* Wavefront shaping in complex media with a 350 kHz modulator via a 1D-to-2D transform. *Nature Photonics* **13**, 788–793 (2019).

[68] Sun, J., Timurdogan, E., Yaacobi, A., Hosseini, E. S. & Watts, M. R. Large-scale nanophotonic phased array. *Nature* **493**, 195–199 (2013).

[69] Chung, S., Abediasl, H. & Hashemi, H. A monolithically integrated large-scale optical phased array in silicon-on-insulator CMOS. *IEEE Journal of Solid-State Circuits* **53**, 275–296 (2017).

[70] Poulton, C. V. *et al.* Long-range LiDAR and free-space data communication with high-performance optical phased arrays. *IEEE Journal of Selected Topics in Quantum Electronics* **25**, 1–8 (2019).

[71] Rogers, C. *et al.* A universal 3D imaging sensor on a silicon photonics platform. *Nature* **590**, 256–261 (2021).

[72] Wang, Q. *et al.* Optically reconfigurable metasurfaces and photonic devices based on phase change materials. *Nature photonics* **10**, 60–65 (2016).

[73] Zhang, Y. *et al.* Electrically reconfigurable non-volatile metasurface using low-loss optical phase-change material. *Nature Nanotechnology* **16**, 661–666 (2021).

[74] Wang, Y. *et al.* Electrical tuning of phase-change antennas and metasurfaces. *Nature Nanotechnology* **16**, 667–672 (2021).

[75] Arbabi, E. *et al.* MEMS-tunable dielectric metasurface lens. *Nature communications* **9**, 1–9 (2018).

[76] Smolyaninov, A., El Amili, A., Vallini, F., Pappert, S. & Fainman, Y. Programmable plasmonic phase modulation of free-space wavefronts at gigahertz rates. *Nature Photonics* **13**, 431–435 (2019).

[77] Wu, P. C. *et al.* Dynamic beam steering with all-dielectric electro-optic III-V multiple-quantum-well metasurfaces. *Nature communications* **10**, 1–9 (2019).

[78] Park, J. *et al.* All-solid-state spatial light modulator with independent phase and amplitude control for three-dimensional LiDAR applications. *Nature nanotechnology* **16**, 69–76 (2021).

[79] Shirmanesh, G. K., Sokhoyan, R., Wu, P. C. & Atwater, H. A. Electro-optically tunable multifunctional metasurfaces. *ACS nano* **14**, 6912–6920 (2020).

[80] Benea-Chelmus, I.-C. *et al.* Electro-optic spatial light modulator from an engineered organic layer. *Nature communications* **12**, 1–10 (2021).

[81] Kim, T. *et al.* A single-chip optical phased array in a wafer-scale silicon photonics/CMOS 3D-integration platform. *IEEE Journal of Solid-State Circuits* **54**, 3061–3074 (2019).

[82] Poulton, C. V. *et al.* 8192-element optical phased array with 100° steering range and flip-chip CMOS. In *CLEO: Applications and Technology*, JTh4A–3 (Optical Society of America, 2020).

[83] Fatemi, R., Khachaturian, A. & Hajimiri, A. A nonuniform sparse 2D large-FOV optical phased array with a low-power PWM drive. *IEEE Journal of Solid-State Circuits* **54**, 1200–1215 (2019).

[84] Ito, H. *et al.* Wide beam steering by slow-light waveguide gratings and a prism lens. *Optica* **7**, 47–52 (2020).

[85] Zhang, X., Kwon, K., Henriksson, J., Luo, J. & Wu, M. C. A large-scale microelectromechanical-systems-based silicon photonics LiDAR. *Nature* **603**, 253–258 (2022).

[86] Huang, Y.-W. *et al.* Gate-tunable conducting oxide metasurfaces. *Nano letters* **16**, 5319–5325 (2016).

[87] Shuai, Y.-C. *et al.* Coupled bilayer photonic crystal slab electro-optic spatial light modulators. *IEEE Photonics Journal* **9**, 1–11 (2017).

[88] Ye, X. *et al.* High-speed programmable lithium niobate thin film spatial light modulator. *Optics Letters* **46**, 1037–1040 (2021).

[89] Vercruysse, D., Sapra, N. V., Yang, K. Y. & Vuckovic, J. Inverse-designed photonic crystal circuits for optical beam steering. *ACS Photonics* **8**, 3085–3093 (2021).

[90] Tamanuki, T., Ito, H. & Baba, T. Thermo-optic beam scanner employing silicon photonic crystal slow-light waveguides. *Journal of Lightwave Technology* **39**, 904–911 (2021).

[91] Sakata, R. *et al.* Dually modulated photonic crystals enabling high-power high-beam-quality two-dimensional beam scanning lasers. *Nature communications* **11**, 1–10 (2020).

[92] Minkov, M. *et al.* Inverse design of photonic crystals through automatic differentiation. *ACS Photonics* **7**, 1729–1741 (2020).

[93] Andreani, L. C. & Gerace, D. Photonic-crystal slabs with a triangular lattice of triangular holes investigated using a guided-mode expansion method. *Physical Review B* **73**, 235114 (2006).

[94] Panuski, C., Englund, D. & Hamerly, R. Fundamental thermal noise limits for optical microcavities. *Physical Review X* **10**, 041046 (2020).

[95] Chen, C. J. *et al.* Selective tuning of high-Q silicon photonic crystal nanocavities via laser-assisted local oxidation. *Optics express* **19**, 12480–12489 (2011).

[96] Lie, L. N., Razouk, R. R. & Deal, B. E. High pressure oxidation of silicon in dry oxygen. *Journal of The Electrochemical Society* **129**, 2828 (1982).

[97] Carreira, J. *et al.* Gigabit per second visible light communication based on algainp red micro-led micro-transfer printed onto diamond and glass. *Optics Express* **28**, 12149–12156 (2020).
[98] Shaltout, A. M. *et al.* Spatiotemporal light control with frequency-gradient metasurfaces. *Science* **365**, 374–377 (2019).
[99] Bogaerts, W. *et al.* Programmable photonic circuits. *Nature* **586**, 207–216 (2020).
[100] Pahlevaninezhad, H. *et al.* Nano-optic endoscope for high-resolution optical coherence tomography in vivo. *Nature photonics* **12**, 540–547 (2018).
[101] Watts, M. R., Shaw, M. J. & Nielson, G. N. Microphotonic thermal imaging. *Nature Photonics* **1**, 632–634 (2007).
[102] Grace, M. R., Dutton, Z., Ashok, A. & Guha, S. Approaching quantum-limited imaging resolution without prior knowledge of the object location. *JOSA A* **37**, 1288–1299 (2020).
[103] Hamerly, R., Bernstein, L., Sludds, A., Soljačić, M. & Englund, D. Large-scale optical neural networks based on photoelectric multiplication. *Physical Review X* **9**, 021032 (2019).
[104] Wetzstein, G. *et al.* Inference in artificial intelligence with deep optics and photonics. *Nature* **588**, 39–47 (2020).
[105] Mosk, A. P., Lagendijk, A., Lerosey, G. & Fink, M. Controlling waves in space and time for imaging and focusing in complex media. *Nature photonics* **6**, 283–292 (2012).
[106] Yoon, S. *et al.* Deep optical imaging within complex scattering media. *Nature Reviews Physics* **2**, 141–158 (2020).
[107] Bourassa, J. E. *et al.* Blueprint for a scalable photonic fault-tolerant quantum computer. *Quantum* **5**, 392 (2021).
[108] Kok, P. *et al.* Linear optical quantum computing with photonic qubits. *Reviews of modern physics* **79**, 135 (2007).
[109] Bartolucci, S. *et al.* Fusion-based quantum computation. *arXiv preprint arXiv:2101.09310* (2021).
[110] Heuck, M., Jacobs, K. & Englund, D. R. Controlled-phase gate using dynamically coupled cavities and optical nonlinearities. *Physical review letters* **124**, 160501 (2020).
[111] Krastanov, S. *et al.* Room-temperature photonic logical qubits via second-order nonlinearities. *Nature communications* **12**, 1–10 (2021).
[112] Aflatouni, F., Abiri, B., Rekhi, A. & Hajimiri, A. Nanophotonic projection system. *Optics express* **23**, 21012–21022 (2015).
[113] Junique, S. *et al.* GaAs-based multiple-quantum-well spatial light modulators fabricated by a wafer-scale process. *Applied optics* **44**, 1635–1641 (2005).
[114] Horie, Y., Arbabi, A., Arbabi, E., Kamali, S. M. & Faraon, A. High-speed, phase-dominant spatial light modulation with silicon-based active resonant antennas. *Acs Photonics* **5**, 1711–1717 (2017).
[115] Yaacobi, A. *et al.* Integrated phased array for wide-angle beam steering. *Optics letters* **39**, 4575–4578 (2014).
[116] Bartlett, T. A., McDonald, W. C. & Hall, J. N. Adapting Texas Instruments DLP technology to demonstrate a phase spatial light modulator. In *Emerging Digital Micromirror Device Based Systems and Applications XI*, vol. 10932, 109320S (International Society for Optics and Photonics, 2019).
[117] Shrauger, V. & Warde, C. Development of a high-speed high-fill-factor phase-only spatial light modulator. In *Diffractive and Holographic Technologies for Integrated Photonic Systems*, vol. 4291, 101–108 (International Society for Optics and Photonics, 2001).
[118] Li, J., Yu, P., Zhang, S. & Liu, N. Electrically-controlled digital metasurface device for light projection displays. *Nature communications* **11**, 1–7 (2020).
[119] Marshel, J. H. *et al.* Cortical layer–specific critical dynamics triggering perception. *Science* **365**, eaaw5202 (2019).
[120] McKnight, D. J., Johnson, K. M. & Serati, R. A. 256× 256 liquid-crystal-on-silicon spatial light modulator. *Applied Optics* **33**, 2775–2784 (1994).
[121] Dostart, N. *et al.* Serpentine optical phased arrays for scalable integrated photonic lidar beam steering. *Optica* **7**, 726–733 (2020).
[122] Jayatilleka, H. *et al.* Post-fabrication trimming of silicon photonic ring resonators at wafer-scale. *Journal of Lightwave Technology* **39**, 5083–5088 (2021).
[123] Biryukova, V., Sharp, G. J., Klitis, C. & Sorel, M. Trimming of silicon-on-insulator ring-resonators via localized laser annealing. *Optics Express* **28**, 11156–11164 (2020).
[124] Hagan, D. E., Torres-Kulik, B. & Knights, A. P. Post-fabrication trimming of silicon ring resonators via integrated annealing. *IEEE Photonics Technology Letters* **31**, 1373–1376 (2019).
[125] Han, S. & Shi, Y. Post-fabrication trimming of photonic crystal nanobeam cavities by electron beam irradiation. *Optics Express* **26**, 15908–15913 (2018).
[126] Gil-Santos, E. *et al.* Scalable high-precision tuning of photonic resonators by resonant cavity-enhanced photoelectrochemical etching. *Nature communications* **8**, 1–7 (2017).
[127] Spector, S., Knecht, J. M. & Juodawlkis, P. W. Localized in situ cladding annealing for post-fabrication trimming of silicon photonic integrated circuits. *Optics Express* **24**, 5996–6003 (2016).
[128] Lipka, T., Kiepsch, M., Trieu, H. K. & Müller, J. Hydrogenated amorphous silicon photonic device trimming by UV-irradiation. *Optics express* **22**, 12122–12132 (2014).
[129] Atabaki, A. H., Eftekhar, A. A., Askari, M. & Adibi, A. Accurate post-fabrication trimming of ultra-compact resonators on silicon. *Optics express* **21**, 14139–14145 (2013).
[130] Cai, T., Bose, R., Solomon, G. S. & Waks, E. Controlled coupling of photonic crystal cavities using photochromic tuning. *Applied Physics Letters* **102**, 141118 (2013).
[131] Hennessy, K., Högerle, C., Hu, E., Badolato, A. & Imamoğlu, A. Tuning photonic nanocavities by atomic force microscope nano-oxidation. *Applied physics letters* **89**, 041118 (2006).

Extended Data

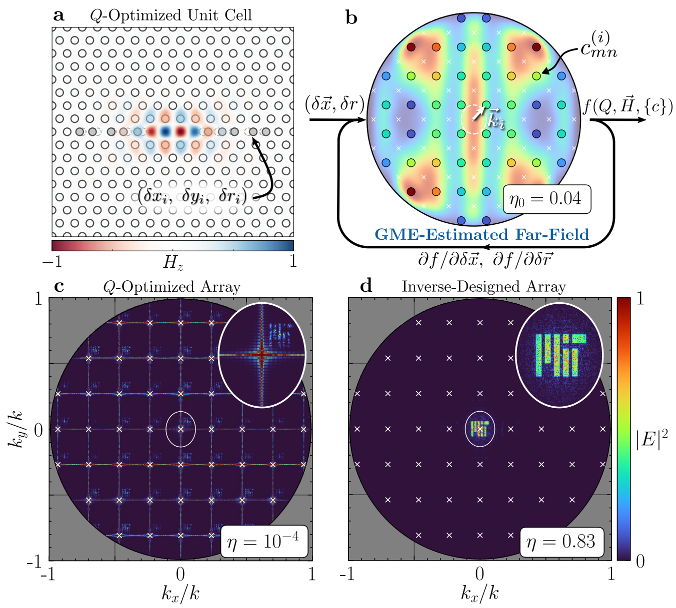

Figure E1: **Optimized holography with inverse-designed, vertically-coupled microcavity arrays.** (a) Silicon $L3$ slab defect cavity design (hexagonal lattice constant $a = 0.4$ µm; hole radius $r/a = 0.25$; slab thickness $t = 220$ nm) with overlaid midplane magnetic field profile H_z after Q optimization by displacing $(\delta x_i,\ \delta y_i)$ and resizing (δr_i) the shaded holes in the $16a \times 16(\sqrt{3}/2)a$ periodic unit cell. Hole shifts are magnified by 3× for visualization. The confined cavity mode radiates into the broad far-field profile in (b, background), violating (C1) and yielding a zero-order diffraction efficiency $\eta_0 \ll 1$. As a result, simulated trial holograms (c) from a 64×64 cavity array with optimized detunings (Supplement Section D) have minimal overall diffraction efficiency η. Inverse design (b) solves these problems. Guided mode expansion (GME) approximates the mode's Q *and* far-field profile by sampling the losses $\{c\}$ at the array's diffraction orders (white ×s) displaced by Bloch boundary conditions $\vec{k}_i$ (i.e. at the colored dots). An objective function f that maximizes Q, confines $\vec{H}$, and minimizes $\{c\}$ at any non-zero diffraction order can then be efficiently optimized with respect to *all* hole parameters using reverse-mode automatic differentiation (b). The resulting devices with high-Q, efficient coupling, and directional emission enable high-performance ($\eta \sim 1$) resonant holography (d).

Class [Year]	**Device**	$N_x \times N_y$	$\Omega_s = \frac{\lambda}{\Lambda_x} \times \frac{\lambda}{\Lambda_y}$	ζ [%]	$\omega_s/2\pi$ [Hz]
EO [2022]	**PhC-SLM**	$\mathbf{8 \times 8}$	$\mathbf{10.6^\circ \times 14.5^\circ}$	**64**	$\mathbf{1.4 \times 10^8}$
EO [2021]	$\chi^{(2)}$ polymer-coated grating [80]	2×2	$0.2^\circ \times 0.2^\circ$	—	5.0×10^7
EO [2019]	$\chi^{(3)}$ thin-film plasmonic resonator [76]	4×4	$0.8^\circ \times 1.1^\circ$	20*	1.0×10^9
EO [2017]	Bilayer guided resonators [87]	6×6	$0.3^\circ \times 0.3^\circ$	40*	2×10^8
EO [2015]	Waveguided p-i-n modulators [112]	4×4	$1.8^\circ \times 1.8^\circ$	10*	2×10^8
EO [2011]	$\chi^{(2)}$ polymer-coated grating [64]	4×4	$0.1^\circ \times 0.1^\circ$	18*	8.0×10^5
EO [2005]	MQW micropillar modulators [113]	128×128	$1.3^\circ \times 1.3^\circ$	50	1.3×10^7
Thermal [2018]	Asymmetric Fabry-Perot cavity [35]	6×6	$3.4^\circ \times 3.4^\circ$	59	1.4×10^4
Thermal [2013]	Waveguided phased array [12, 115]	8×8	$9.9^\circ \times 9.9^\circ$	10*	1.1×10^5
MEMS [2019]	Grating phase shifters [66]	160×160	$4.4^\circ \times 4.1^\circ$	85*	5.5×10^4
MEMS [2019]	Piston mirrors [116]	960×540	$3.4^\circ \times 3.4^\circ$	—	2.0×10^4
MEMS [2014]	High-contrast gratings [65]	8×8	$2.7^\circ \times 2.7^\circ$	36*	5.0×10^5
MEMS [2001]	Piston mirrors [117]	256×256	$0.9^\circ \times 0.9^\circ$	86	5.0×10^5
LC [2020]	Plasmonic metasurface [118]	3×2	$0.3^\circ \times 0.3^\circ$	—	2.5×10^1
LC [2019]	"MacroSLM" [119]	1536×1536	$3.0^\circ \times 3.0^\circ$	95	6.0×10^2
LC [1994]	Binary ferroelectric LC [120]	256×256	$2.2^\circ \times 2.2^\circ$	79	8.3×10^3

Table E1: Performance comparison of our PhC-SLM (bold) to selected active 2D spatial light modulators from Fig. 1b. Estimated fill factors ζ are marked by a *. Wavelength-steered devices [121] are excluded to focus on active, individually-addressable arrays.

Technique [Year]	**Cavity Type**	N	$\Delta\lambda_0^{\text{p-p}}$ [pm]	$\langle Q \rangle$	**In situ?**	**Parallel?**
"Holographic" oxidation [2022]	**Si PhC**	**64**	**13**	2×10^5	**Y**	**Y**
Germanium implantation [2021]	Si ring [122]	58	32	4×10^3	Y	N
Laser-annealed cladding [2020]	Si ring [123]	2	20*	2×10^4	Y	N
Boron implantation [2019]	Si ring [124]	4	15	5×10^3	Y	N
Electron-beam irradiation [2018]	Si PhC [125]	4	400	3×10^5	N	N
Photo-electro-chemical etching [2017]	GaAs disk [126]	5	200*	2×10^4	Y	N
Annealed cladding [2016]	Si ring [127]	5	90*	3×10^3	Y	N
Ultraviolet irradiation [2014]	a-Si ring [128]	4	45	8×10^3	Y	N
Post-fabrication etching [2013]	GaAs PhC [129]	18	100*	3×10^4	N	Y
Photochromatic thin-film [2011]	GaAs PhC [130]	3	340	8×10^3	Y	N
Anodic oxidation [2006]	GaAs PhC [131]	2	100*	5×10^3	N	N

Table E2: Comparison of previous microcavity array trimming techniques to our parallel laser assisted thermal oxidation (bold). Estimated values are marked with a *. $\Delta\lambda_{\text{p-p}}$ = peak-to-peak wavelength error; $\langle Q \rangle$ = mean quality factor.

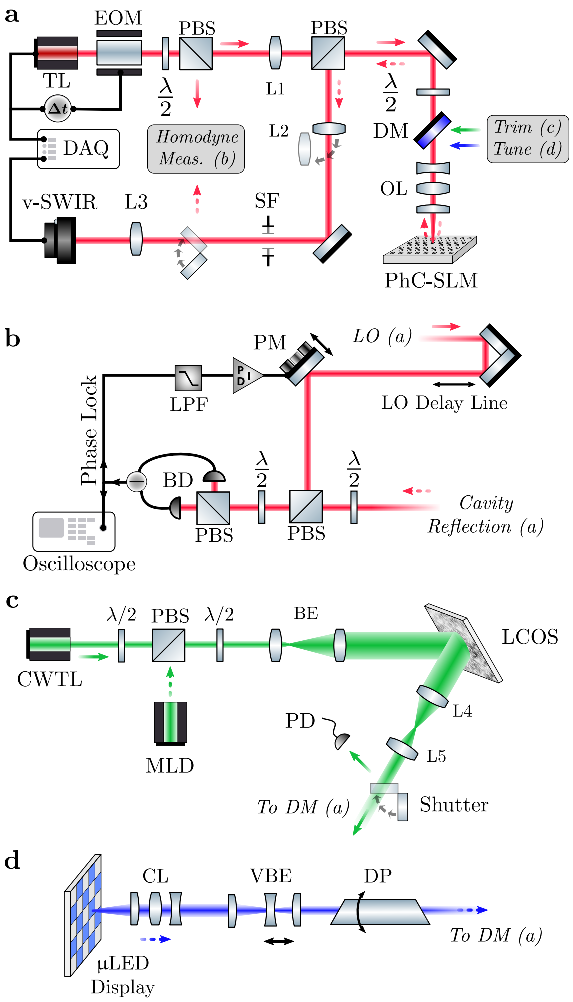

Figure E2: Overview of experimental setups for measuring and controlling the photonic crystal SLM (PhC-SLM). A cross-polarized microscope (a) featuring balanced homodyne measurement (b) enables near- and far-field characterization of cavity arrays controlled by SLM-distributed coherent light (c) or high-speed incoherent μLED arrays (d). TL: tunable infrared laser (Santec TSL-710), EOM: electro-optic amplitude modulator; $\lambda/2$: half-wave plate, PBS: polarizing beamsplitter; L1: 250 mm back-focal-plane lens; DM: long-pass dichroic mirror; OL: objective lens (Nikon Plan Fluor 40×/0.60 NA or Nikon LU Plan 100×/0.95 NA), L2: 250 mm back-focal-plane lens; SF: spatial filter; L3: 200 mm tube lens; v-SWIR: visible-short wave infrared camera (Xenics Cheetah 640); DAQ: data acquisition unit (NI USB-6343); Δt: trigger delay generator (SRS DG645); LO: local oscillator; PM: piezo mirror; BD: balanced detector (Thorlabs PDB480C-AC); Phase Lock: TEM LaseLock; LPF: low-pass filter; CWTL: continuous-wave trimming laser (Coherent Verdi V18); MLD: modulated laser diode (Hubner Cobolt or PicoLAS LDP); BE: 5× visible beam expander; LCOS: high-power liquid crystal SLM (Santec SLM-300); L4: 300 mm; L5: 250 mm; PD: photo-detector; CL: collection lens (Zeiss Fluar 5×/0.25 NA); VBE: 0.5 × −2× variable beam expander; DP: dove prism.

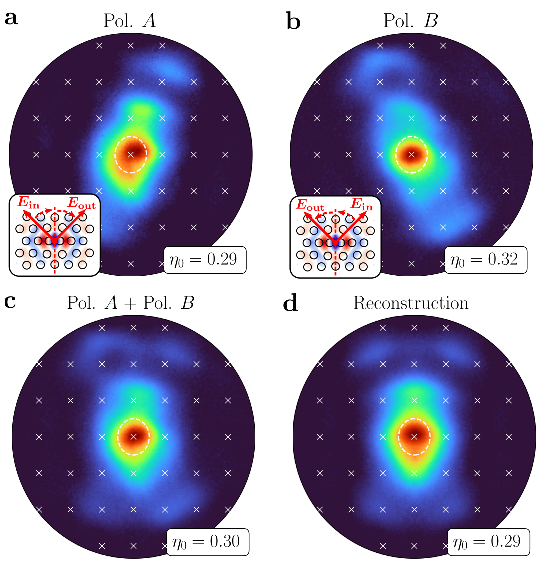

Figure E3: Cross-polarized back-focal-plane (BFP) imaging techniques for a grating-coupled $L3$ cavity. Two orthogonally polarized far-field profiles are imaged by orienting the input polarization E_{in} at a $+45°$ (a) or $-45°$ (b) angle from the dominant cavity polarization axis (dashed line in inset). The complete cavity emission profile $S(\vec{k})$ can be reconstructed by summing both images (c) or approximated from a single polarized image (d), yielding near-identical images with quantitative agreement between the extracted η_0.

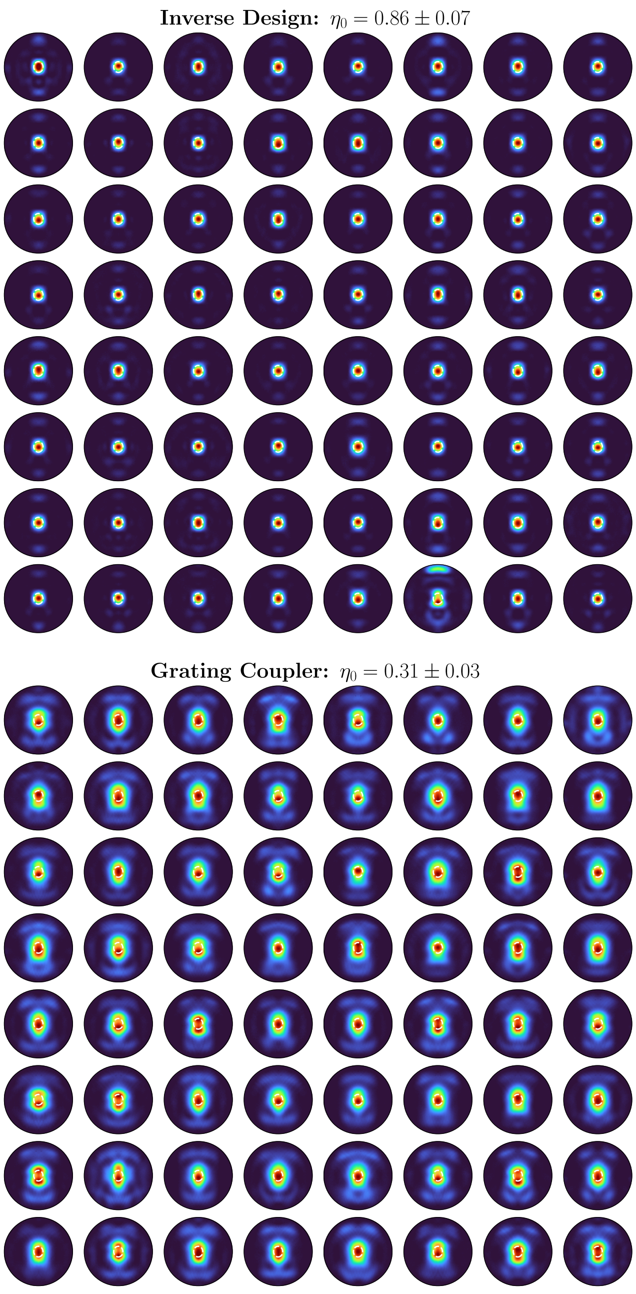

Figure E4: Imaged far-field profiles $S(\vec{k})$ (over a 0.9 numerical aperture) for each device in an 8×8 array of inverse designed (top) and grating-coupled (bottom) $L3$ PhC cavities. The extracted zero-order efficiencies η_0 and standard deviations are also provided.

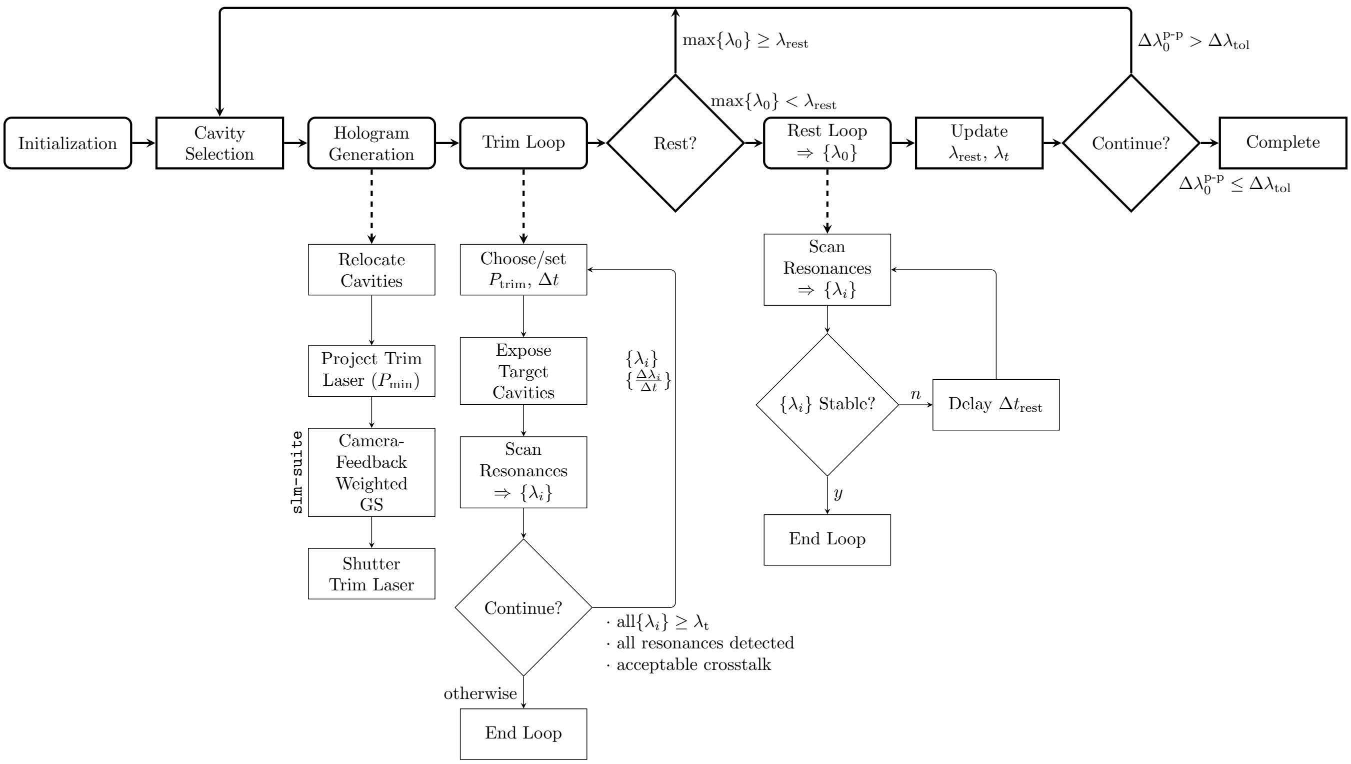

Figure E5: Flowchart of the holographic trimming algorithm. Trimming holograms are formed with weighted Gerchberg-Saxton (GS) algorithms and projected onto desired cavities for duration Δt with power P_{trim}. Alternating trimming and resonance readout periods continue until the instantaneous wavelength λ_i of any targeted cavity blueshifts past the target wavelength λ_t. Thereafter, a new set of target cavities is selected and trimmed. This selection and trimming sub-loop continues until all resonant wavelengths $\{\lambda_0\}$ are below the "rest" wavelength λ_{rest}, at which point trimming is halted and the resonances are continuously monitored at readout interval Δt_{rest}. When the resonances are sufficiently stable (redshifting from moisture adsorption to the silicon membrane is arrested), the total "rehydration" redshift $\Delta\lambda_0$ of each cavity is updated to better estimate the true resonant wavelength $\lambda_0 \approx \lambda_i + \Delta\lambda_0$ from the instantaneous wavelengths $\{\lambda_i\}$ during trimming. The entire process terminates when the peak-to-peak static resonant wavelength uniformity $\Delta\lambda_0^{\text{p-p}}$ drops below the desired tolerance $\Delta\lambda_{\text{tol}}$.

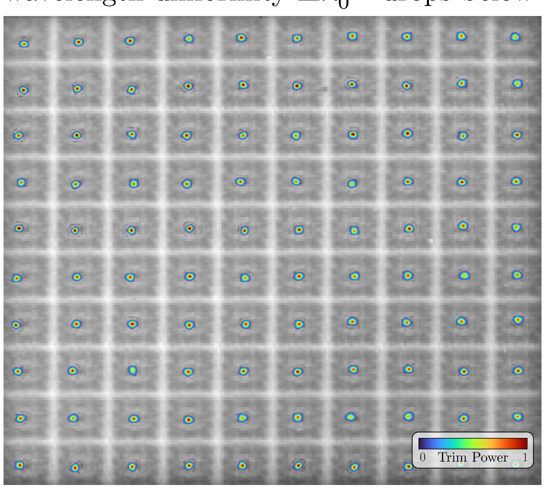

Figure E6: Overlaid images of 10×10 cavity (grey) and trimming spot (color) arrays demonstrating the $\ll$ µm placement accuracy and percent-order power uniformity of weighted Gerchberg-Saxton phase retrieval with experimental camera feedback. In general, our holography software (Supplement Section F) creates high-uniformity optical foci to arbitrary image plane locations specified by the user.